

# Optical and electrochemical study of discrete supramolecular complexes for organic photovoltaic application

by

Mokgadi Josephine Refilwe Mosana

Submitted in fulfilment of the requirements for the degree

Magister Scientiae

In the Faculty of Natural & Agricultural Sciences

University of Pretoria

Pretoria

2022, December

## Declaration

I, Mokgadi Josephine Refilwe Mosana, declare that the dissertation, which I hereby submit for the degree Magister Scientiae at the University of Pretoria, is my work and has not previously been submitted by me for a degree at this or any other tertiary institution.

SIGNATURE: \_\_\_\_\_

DATE: \_\_\_\_\_

## Abstract

Supramolecular complex formation using donor and acceptor macrocycles are important field of research in solar energy harvesting. In this study, multiwalled carbon nanotubes is used as an acceptor and its associative interactions with macrocyclic and polymeric donors such as phthalocyanines (free base H<sub>2</sub> and Mn centred) and Poly[2,6-(4,4-bis-(2-ethylhexyl)-4H-cyclopenta [2,1-b;3,4-b']dithiophene)-alt-4,7(2,1,3-benzothiadiazole)] (PCPDTBT) were studied using absorption and emission spectroscopy, electrochemical methods and transmission electron microscopy. The calculated molar extinction coefficients and fluorescence quantum yield values show that the selected donors not only strongly absorb at high wavelengths but also at lower concentrations they effectively release excited state charge at 600 nm (for phthalocyanines) and 624 nm (for polymeric donor). This is further corroborated by the binding constants obtained during this study. The binding constants as calculated from the spectroscopic methods (ranging from 10<sup>3</sup> to 10<sup>6</sup> for the macrocycles to polymer) with that of electrochemical methods indicated a similar trend. This was further validated by the low-resolution TEM studies which indicated the decoration of MWCNT with the donors used. Thus, MnPc and PCPDTBT were the most stable of the complexes showing a good promise to find application as active materials in organic photovoltaics.

## Acknowledgements

I would like to express my sincere appreciation to my supervisor, Dr SG Radhakrishnan for her support, patience, and guidance. All her efforts to ensure that my journey was bearable, and that our working environment in the group is healthy didn't go unnoticed.

I also would like to convey my thanks to my research group for their support, and willingness to lend me their ears and time even though our projects had different focusses, they never once sent me away but sought to address the questions that rose in my project. Additionally, I am grateful for National Research Foundation (NRF) for funding my research, thus the opportunity to further my studies.

Lastly, I'd like to extend my deepest gratitude to my family and friends for the words of encouragement, steadfast love, and prayers. This journey wouldn't have been possible without them. I am indeed grateful to have them in my life.

# Table of Contents

Declaration .....	I
Abstract .....	II
Acknowledgements .....	III
List of Abbreviations .....	a
List of Figures .....	c
List of Tables .....	f
Chapter 1 Introduction .....	1
1. Introduction .....	1
1.1. Literature review .....	2
1.1.1. Consideration of organic photovoltaic devices .....	2
1.1.2. The configuration of organic photovoltaic devices .....	3
1.1.3. Organic Materials used in organic photovoltaic devices .....	4
1.1.4. The formation of excitons .....	10
1.1.5. Exciton diffusion length .....	11
1.1.6. Exciton separation .....	11
1.2. Materials- Donors and acceptor used in this study .....	13
1.2.1. Acceptor Material: MWCNT .....	13
1.2.2. Donor materials: Phthalocyanines .....	14
1.2.3. Conjugated conducting polymer: PCPDTBT .....	16

Chapter 2 Methodology .....	18
2. Experimental work .....	18
2.1. Absorbance and Fluorescence measurements .....	18
2.2. Electrochemistry measurements .....	19
2.3. Fluorescence quantum yield measurements .....	20
2.4. Transmission Electron Microscopy (TEM) measurements .....	21
Chapter 3 Results and discussion .....	23
3. Spectrophotometric and Voltammetric measurements .....	23
3.1. Uv-vis spectroscopy and molar extinction coefficients of pristine compounds .....	23
3.2. Fluorescence spectroscopy and Quantum Yields .....	26
3.3. Spectrophotometric Titrations .....	30
3.3.1. MWCNT-H <sub>2</sub> Pc titrations .....	30
3.3.2. MWCNT-MnPc titrations .....	31
3.3.3. MWCNT-PCPDTBT titrations .....	31
3.3.4. Acceptor-Donor Binding Constants, K .....	32
3.4. Electrochemical Measurements .....	34
3.4.1. Cyclic voltammetry and Differential Pulse Voltammogram (DPV) of pristine donors (H <sub>2</sub> Pc, MnPc and PCPDTBT) .....	34
3.4.2. DPV Measurements for A-D complexes .....	38
3.4.3. Electrochemical Acceptor-Donor Binding Constants, K .....	41
3.5. Transmission electron microscopy measurements .....	42
Chapter 4 .....	45
4. Conclusions and Future work .....	45
4.1. Conclusions .....	45

4.2. Future work ..... 45

References ..... 46

## List of Abbreviations

HOMO	Highest Occupied Molecular Orbital
LUMO	Lowest Unoccupied Molecular Orbital
EtOH	Ethanol
Rh-6G	Rhodamine 6G
UV-vis	Ultraviolet visible
OPV	Organic Photovoltaic
IR	Infrared
A-D	Acceptor-Donor
CT	Charge transfer
$V_{oc}$	Open-circuit voltage
CO <sub>2</sub>	Carbon dioxide
$D$	Diffusion length
$\tau$	Exciton lifetime
$L_D$	Exciton diffusion length
Fe	Iron
Si	Silicon
Al	Aluminium
Mg	Magnesium
TM	Transition metal
Ca	Calcium
Co	Cobalt
kV	kilovolts
RT	Room temperature
C <sub>60</sub>	Fullerene
ITO	Indium Tin Oxide
OPV	Organic Photovoltaic
PV	Photovoltaic
PCE	Power conversion efficiency
PHJ	Planar heterojunction



BHJ	Bulk heterojunction
CuPc	copper phthalocyanine
CP	Conjugated polymer
SM	Small molecule
PTBEHT	Poly {5,7-di-2-thienyl-2,3-bis(3,5-di(2-ethylhexyloxy)phenyl)-thieno[3,4-b]pyrazine}
P3HS	Poly(3-hexyl) selenophene)
PBEHTT	Poly {5,7-bis[3, 4-di(2-ethylhexyloxy)- 2-thienyl]-2, 3-diphenyl-thieno[3,4-b]pyrazine}
MDMO-PPV	Poly[2-methoxy-5-(3',7'-dimethyloctyloxy)-1,4-phenylenevinylene]
MEH-PPV	Poly[2-methoxy-5-(2'-ethylhexyloxy)-1,4-phenylene vinylene]
P3HT	Poly(3-hexylthiophene)
PCPDTBT	Poly[2,6-(4,4-bis-(2-ethylhexyl)-4H-cyclopenta [2,1-b;3,4-b']dithiophene)-alt-4,7(2,1,3-benzothiadiazole)]
FBR	5,5'-[(9,9-Dioctyl-9H-fluorene-2,7-diyl)bis(2,1,3-benzothiadiazole-7,4-diylmethylidyne)]bis[3-ethyl-2-thioxo-4-thiazolidinone]
PCBM	Phenyl-C <sub>61</sub> butyric acid methyl ester
$\lambda_{\text{ex}}$	Excitation wavelength
eV	Electron volt
$\epsilon_0$	Molar extinction coefficient
CBZ	chlorobenzene
<i>o</i> DCB	<i>ortho</i> -dichlorobenzene
mm	Millimetre
nm	nanometre
mV	Millivolts
mV/s	millivolts per second
mg/mL	Milligrams per millilitre
ppm	Parts per million

SCE	Saturated Calomel Electrode
NHE	Standard Hydrogen Electrode
TBA-PF <sub>6</sub>	Tetrabutylammonium hexafluorophosphate
P3OT	Poly(3-octylthiophene-2,5-diyl)
Fc/Fc <sup>+</sup>	Ferrocene to Ferrocenium ion

## List of Figures

Figure 1.	A typical dispersed settlement in a South African rural area .....	2
Figure 2a.	The single layer based OPV configuration .....	3
Figure 2b.	The planar heterojunction (PHJ) OPV configuration .....	3
Figure 3.	Bulk heterojunction (BHJ) OPV configuration .....	4
Figure 4.	Schematic showing the formation of excitons after absorbing photons .....	10
Figure 5.	Diagram showing the processes that occurs in (a) planar/or bilayer heterojunction (PHJ), and (b) bulk heterojunction (BHJ) systems. (b) The dashed lines show both the HOMO and LUMO energy levels.....	12
Figure 6.	Molecular structure of (a) Single-walled carbon nanotube (SWCNT) and (b) Multiwalled carbon nanotube (MWCNT) .....	14
Figure 7.	Molecular structure of metal-free phthalocyanine (H <sub>2</sub> Pc) (a) and manganese II phthalocyanine (MnPc) (b) .....	15
Figure 8.	Molecular structure of PCPDTBT (a) and P3HT (b) .....	17
Figure 9.	A plot of energy band gaps of the acceptor and donor materials considered for this project .....	17
Figure 10.	A three-electrode cell setup.....	20
Figure 11.	Transmission electron microscope (TEM) diagram .....	22

Figure 12. Left: Uv-vis absorption spectrum of varying concentrations H<sub>2</sub>Pc (0.5 to 5.5 x10<sup>-4</sup> M; indicated by traces purple to dark red) in CBZ; Right: Absorbance against concentration of H<sub>2</sub>Pc for the calculation of molar extinction coefficient at 347 nm ..... 23

Figure 13. Left: Uv-vis absorption spectrum of varying concentrations MnPc (0.35 to 3.5 x10<sup>-5</sup> M, indicated by traces purple to dark red) in CBZ; Right: Absorbance against concentration of MnPc for the calculation of molar extinction coefficient at 359 nm ..... 24

Figure 14. Left: Uv-vis absorption spectrum of varying concentrations PCPDTBT (3.0 to 7.0 x10<sup>-7</sup> M; indicated by traces purple to dark red) in CBZ; Right: Absorbance against concentration of PCPDTBT for the calculation of molar extinction coefficient at 410 nm ..... 25

Figure 15. The UV-vis absorption spectrum of 0.1 mg/mL MWCNT recorded in CBZ ..... 25

Figure 16. Left: Fluorescence spectrum of H<sub>2</sub>Pc (0.5 to 5.5 x10<sup>-4</sup>M; indicated by traces purple to dark red) in CBZ; Right: Linear plot of absorbance against integrated fluorescence of H<sub>2</sub>Pc in CBZ to calculate fluorescence quantum yield excited at 600 nm ..... 27

Figure 17. Left: Fluorescence spectrum of MnPc (0.35 to 3.5 x10<sup>-5</sup> M; indicated by traces purple to dark red) in CBZ; Right: Linear plot of absorbance against integrated fluorescence of MnPc in CBZ to calculate fluorescence quantum yield excited at 600 nm ..... 28

Figure 18: Left: fluorescence spectrum of PCPDTBT (3.0 to 7.0 x10<sup>-7</sup>M; indicated by traces purple to dark red) in CBZ; Right: Linear plot of absorbance against \integrated fluorescence of PCPDTBT in CBZ to calculate fluorescence quantum yield excited at 624 nm ..... 28

Figure 19: Spectral changes upon the addition of variable concentration of H<sub>2</sub>Pc (0 to 7 x10<sup>-4</sup>M) to 0.05 mg/mL of MWCNT in CBZ. Left: Absorption Spectrum; Right: Emission Spectrum,  $\lambda_{ex} = 650$  nm ..... 30

Figure 20:	Spectral changes upon the addition of variable concentration of MnPc (0 to $5 \times 10^{-5}$ M) to 0.05 mg/mL of MWCNT in CBZ. Left: Absorption Spectrum; Right: Emission Spectrum, $\lambda_{ex} = 650$ nm .....	31
Figure 21:	Spectral changes upon the addition of variable concentration of PCPDTBT (0 to $9 \times 10^{-7}$ M) to 0.05 mg/mL of MWCNT in CBZ. Left: Absorption Spectrum; Right: Emission Spectrum, $\lambda_{ex} = 650$ nm .....	32
Figure 22:	A plot of $A_o/A_o-A$ vs. inverse conversation of the donor – (a) H <sub>2</sub> Pc, (b) MnPc, (c) PCPDTBT and $I_o/I_o-I$ vs. inverse concentration of the donor – (d) H <sub>2</sub> Pc, (e) MnPc, (f) PCPDTBT, at a constant MWCNT concentration (0.05 mg/mL) collected in CBZ solvent .....	33
Figure 23:	DPV of H <sub>2</sub> Pc; Conc. $1.16 \times 10^{-4}$ M; DPV parameters: pulse height: 10 mV, scan rate 0.01 V/s .....	35
Figure 24:	DPV of MnPc; Conc. $9.83 \times 10^{-5}$ M; DPV parameters: pulse height: 10 mV, scan rate 0.01 V/s .....	36
Figure 25:	DPV of PCPDTBT; Conc. $1.23 \times 10^{-6}$ M; DPV parameters: pulse height: 10 mV, scan rate 0.01 V/s .....	37
Figure 26:	Differential pulse voltammogram of H <sub>2</sub> Pc ( $1 \times 10^{-4}$ M) with variable concentration of MWCNT (0 – 3 mL aliquots of 0.05 mg/mL) at 10 mV pulse amplitude, 10 mV/s scan rate on a glassy carbon electrode in oDCB: TBA-PF <sub>6</sub> solution; The inset shows the zoomed in DPV of H <sub>2</sub> Pc indicating the movement of anodic peak .....	38
Figure 27:	Differential pulse voltammogram of MnPc ( $1 \times 10^{-4}$ M) with variable concentration of MWCNT (0 – 3 mL aliquots of 0.05 mg/mL) at 10 mV pulse amplitude, 10 mV/s scan rate on a glassy carbon electrode in oDCB: TBA-PF <sub>6</sub> solution; The inset shows the zoomed in DPV of MnPc indicating the movement of anodic peak .....	40
Figure 28:	Differential pulse voltammogram of PCPDTBT ( $1 \times 10^{-4}$ M) with variable concentration of MWCNT (0 – 4 mL aliquots of 0.05 mg/mL) at 10 mV pulse amplitude, 10 mV/s scan rate on a glassy carbon electrode in oDCB: TBA-PF <sub>6</sub>	

	solution; The inset shows the zoomed in DPV of PCPDTBT indicating the movement of anodic peak .....	41
Figure 29.	TEM image of H <sub>2</sub> Pc – MWCNT complex taken at the concentration where crossover was observed in absorption measurements. Please refer to the explanation in the main text for (a) and (b) .....	43
Figure 30	TEM image of MnPc – MWCNT complex taken at the concentration where crossover was observed in absorption measurements. The inset shows the zoomed portion of one of the selected darker areas which reveal the presence of MWCNT .....	43
Figure 31	TEM image of PCPDTBT – MWCNT complex taken at the concentration where crossover was observed in absorption measurements. The right image shows the zoomed portion of one of the selected darker areas which reveal the presence of MWCNT intertwined with PCPDTBT.....	44

## List of Tables

Table 1:	Various organic materials that have been investigated for OPV application...	6
Table 2:	Molar extinction coefficients ( $\epsilon_0$ ) of H <sub>2</sub> Pc, MnPc and PCPDTBT calculated at 679 nm, 724 nm, and 712 nm respectively in CBZ.....	26
Table 3:	The fluorescence quantum yield ( $\Phi_F$ ) of pcs at 600 nm and of PCPDTBT at 624 nm in chlorobenzene (CBZ) and chloroform respectively, measured at RT.....	29
Table 4:	The UV-vis and fluorescence binding constant of complexes that formed at 650nm (absorption and emission) recorded in chlorobenzene.....	33
Table 5:	Optical band gap ( $E_{ga}^{Opt}$ ) and electrical band gap ( $E_{gap}^{Echem}$ ) of pristine donor compounds.....	37
Table 6:	Electrochemical titration of donors with increasing concentration of MWCNT (0 – 3 mL aliquots of 0.05 mg/mL) in oDCB: TBA-PF <sub>6</sub> solution results.....	38
Table 7:	The binding constant (K) from electrochemical titration of donors with increasing concentration of MWCNT in oDCB: TBA-PF <sub>6</sub> solution.....	42

# ***Chapter 1***

## ***1. Introduction***

An estimated 28 gigatons of carbon dioxide (CO<sub>2</sub>) is said to be produced per year, with ~85% accounted to natural gas, oil and coal [1]. The concentrations of CO<sub>2</sub> in the atmosphere has increased from 280 ppm to 384 ppm since industrial revolution [2]. This is due to an increased dependency on the usage of coal-based electricity, particularly in developing countries. Thus the average earth temperature is expected to increase by 2 °C as the concentration of CO<sub>2</sub> increases [3] contributing 80% to global warming compared to other greenhouse gases [4].

Coal-powered electricity is the most common source of electrical energy and is obtained by burning coal and water for cooling which results in the emission of CO<sub>2</sub> and pollution of water [5]. Eskom is the primary electrical energy provider in the Southern Africa [6], making it the largest CO<sub>2</sub> emitter. Likewise, Sasol coal to liquid plants contributed 10% towards South Africa's CO<sub>2</sub> emission in 2020 [7], forming a part of the top greenhouse gas emission contributors in South Africa. Furthermore, South Africa is classified as a semi-arid country (at least 65% of the country) receiving a minimum of 450mm annual average rainfall lower than the world's annual average rainfall that is approximately 850mm; leading to speculated water shortages during the year 2025 [8]. Also, Eskom has been an unreliable energy supplier in most rural areas which struggles without electricity due to the difficulty associated to establishing grid infrastructure in scattered settlement [9], as shown in Figure 1 below a typical dispersed settlement in the rural areas. Additionally, the country is grappled by heavy load shedding schedules with almost no electricity for more than 8 hours per day in urban areas. Therefore, to save the available water sources, reduce annual CO<sub>2</sub> emissions and ensure that energy need in south Africa is addressed, alternative renewable energy sources must be sought as the only viable means to reduce the above-mentioned situations. Since the country receives abundant solar radiation that is highly underutilized, photovoltaic research will play a major role in ameliorating the current problem.



Figure 1. A typical dispersed settlement in a South African rural areas [10].

In this context, the current thesis aims to find an appropriate donor (D)-acceptor (A) system that is capable of forming stable supramolecular complexes. We therefore investigate in this study, the physicochemical interactions of our appropriately chosen D-A systems with help of basic tools such as spectroscopy, electrochemical and surface imaging methods. These methods will shine light on the change/adjustment of LUMO-HOMO energy levels of the D-A systems upon mixing, which is indicative of efficient charge transfer [2] leading to a plausible use as an active layer in the fabrication of organic photovoltaic (OPV) devices.

## 1.1. Literature Review

### 1.1.1. Consideration of organic photovoltaic devices

Until recently silicon (Si)-based photovoltaic (PV) devices were the primary system used in harvesting solar radiation for production of electricity. The first crystalline silicon solar cell was developed in the 1950s with an efficiency of 6% [11]. Since then the efficiency of single Si-based solar cells have increased to over 25.6% [12]. Although the overall Si-based PVs performance is desirable, their manufacture and installation costs are high [13]. Therefore, considering alternative materials that will reduce these costs and wean the dependence on silicon would be beneficial. Organic materials have attracted attention to be used as an active layer of OPVs due to the distinguished attributes such as; being environmentally friendly, cost effective and flexible allowing Roll-to-Roll production over a large area [14].

### 1.1.2. The configuration of the organic photovoltaic devices

When the first fully OPV solar cell, known as homojunction or single layer based solar cells (Figure 2a) were made, the devices could not achieve efficiencies higher than 0.1% [15]. In 1986, a ground breaking discovery made by Tang, [16] completely changed the assemblage of the active layer of OPVs, introducing a novel D-A configuration (also known as planar heterojunction (PHJ) [16]) where two materials with two different electron affinities were combined as shown in Figure 2b. Specifically, copper phthalocyanine (CuPc) as donor material and perylene tetracarboxylic derivative as acceptor material, it was observed that there is charge transfer after irradiation which contributes to the overall photocurrent of the cell reporting efficiency of about 1% [14].

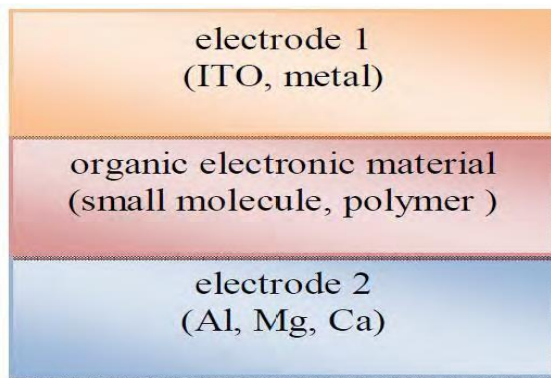


Figure 2a. The single layer based OPV configuration [5].

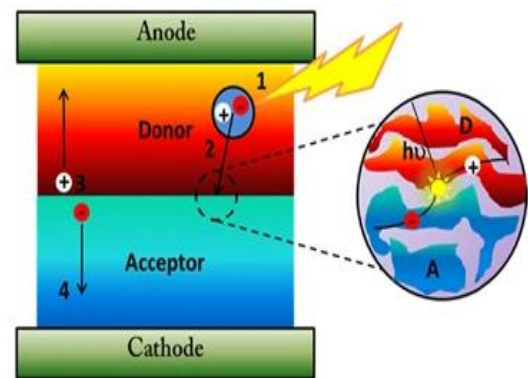


Figure 2b. The planar heterojunction OPV configuration [17].



The discovery of photoinduced charge transfer (CT) between Poly[2-methoxy-5-(2'-ethylhexyloxy)-1,4-phenylene vinylene] (MEH-PPV) and fullerene ( $C_{60}$ ) in a blend not only further revolutionized the assembling of the active layer but also significantly improved the overall performance of OPVs [18]. Mixing of the acceptor and donor materials pioneered the configuration of OPVs to what is now known as bulk heterojunctions (BHJ) (Figure 3). This assemble also showed reduced diffusion length ( $L_D$ ) and increased the exciton dissociation [19] which were previously noted to be some of the drawbacks encountered with PHJ OPV devices [15]. These exceptional properties propelled wide research on conjugated polymer (CP) based OPVs. Yu, et al. [20] assembled the first BHJ that consisted of conjugated polymer donor material MEH-PPV mixed with functionalized  $C_{60}$  as acceptor material, recording energy conversion efficiency of 2.9%. Similarly, Schultes et al. [21] investigated CuPc: $C_{60}$  BHJ observed an improved photoinduced CT thus enhancing the overall performance of the cell. This can be attributed to the continuous network of interpenetrating A-D heterojunctions [19, 20] which increases charge separation; contrary to what is observed with planar heterojunction configuration, where the poor interaction between the donor and acceptor materials was observed [20].

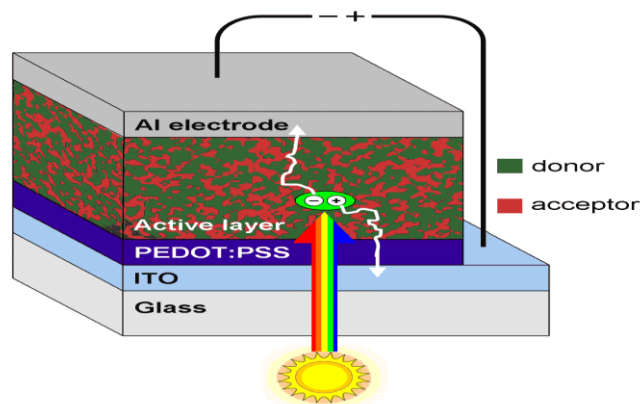


Figure 3. Bulk heterojunction (BHJ) photovoltaic device configuration [5].

### 1.1.3. Organic Materials used in organic photovoltaic devices


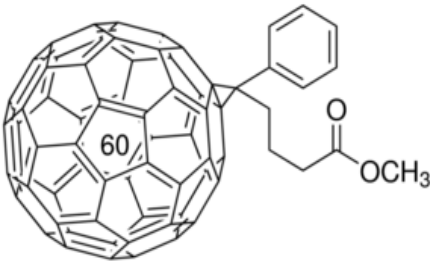
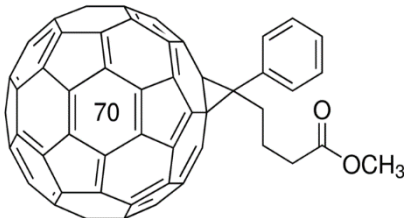
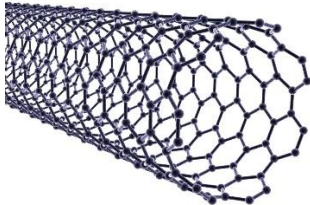
Organic materials used in the active layer of the OPVs are central to the conversion of the absorbed solar radiation into electrical energy thus influence their overall power production not excluding the design of the cell [22]. Therefore, the advancement of OPVs is dependent on the

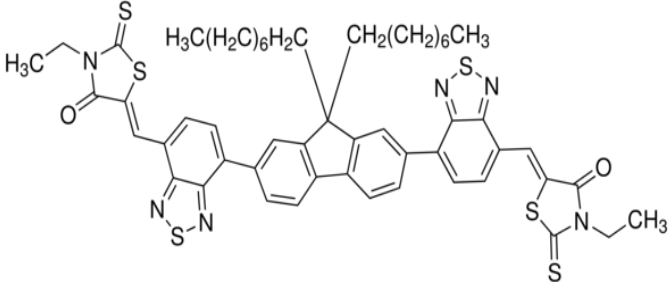
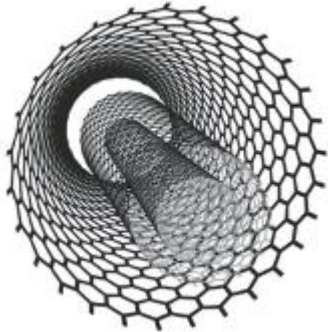
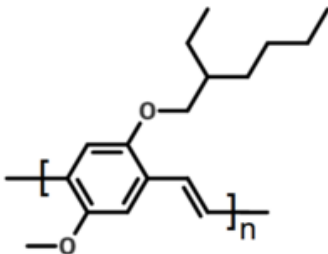
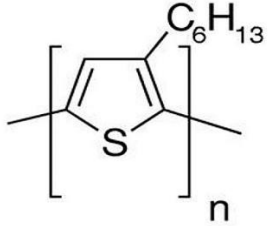
progress made on the fabrication of organic materials [23]. Although there has been a great progress made towards improving their power conversion efficiency (PCE), the limitations displayed by these materials that have currently been investigated inhibits OPVs profitability in the markets [24]. For example, the Poly (3-hexylthiophene) (P3HT): [6,6]-phenyl-C<sub>61</sub> butyric acid methyl ester (PCBM)-based BHJ solar cells is the most studied combination with 1033 journals between the year 2002 and 2010 [25]; reporting promising efficiencies of ~6.82% during this period [26]. However, P3HT's large bandgap allows the material to only harvests 46% of the solar radiation and absorbs wavelengths below 650 nm [27, 28] thus reducing the efficiency of exciton generation, electron transfer (ET) and charge transport [29, 30]. Also, the HOMO-LUMO energy level offsets between P3HT and PCBM is very high [27] leading to the loss of charge. Further the acceptor material PCBM does not effectively absorb in the visible range of the solar spectrum and its bandgap is not tuneable [31]. The material's non-efficient absorption of the photons is observable when mixed with PCPDTBT, there is no notable impact on the donors absorptive properties [32]. Hence, more studies have been focused on investigating other conjugated polymers that have small bandgap and absorbs longer wavelengths [14] without reducing the CT efficiency, including new acceptor materials [31].

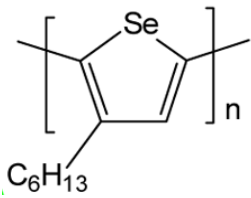
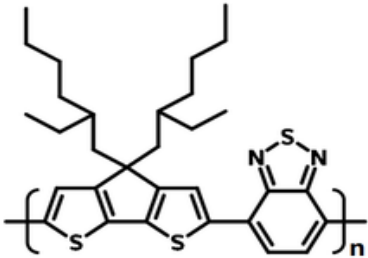
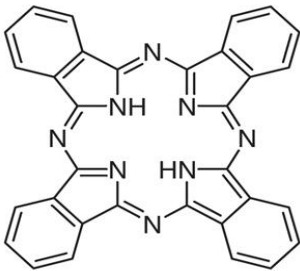
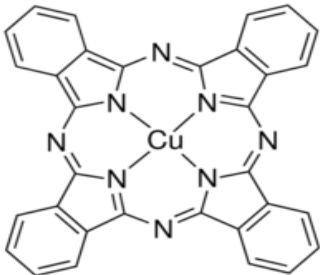
Small molecule (SM) based BHJ devices on the other hand, have not been intensively studied compared to the conjugated polymers; hence their efficiencies continue to lag behind [28, 33]. However, SMs can absorb a wider section of the solar spectrum [34], they can be customized to have smaller bandgaps thus reduced offset energy between the HOMO-LUMO levels [28]. Schultes *et al.* [21] utilized CuPc as a donor absorbing in the range 625 – 694 nm and observed CT in the blend of CuPc:C<sub>60</sub>. Similarly, Holliday *et al.* [35] used small molecular acceptor known as 5,5'-[(9,9-Dioctyl-9H-fluorene-2,7-diyl)bis(2,1,3-benzothiadiazole-7,4-diylmethylidene)]bis[3-ethyl-2-thioxo-4-thiazolidinone] (FBR) in the fabrication of FBR:P3HT BHJ reporting PCE of 4.1% and the SM absorbs at 488 nm thus adding to the overall photocurrent of the cell. Therefore, SMs can be utilized in the fabrication of OPVs and ultimately contribute to the overall energy supply.

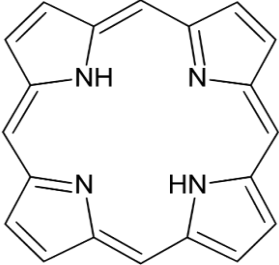
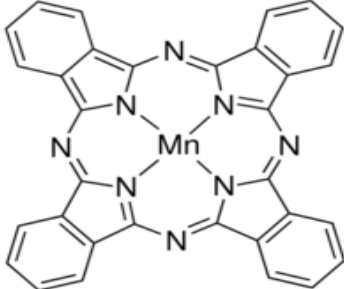
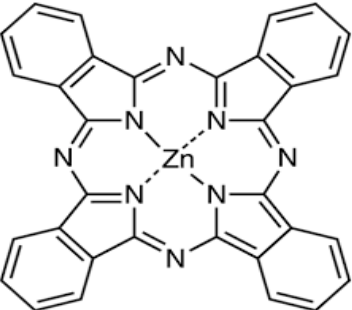
The organic materials used as an active layer in OPVs are chosen based on their solar radiation spectrum collection which is dependent on their band gap (LUMO-HOMO energy levels) (Table 1).

Table 1. Various organic materials that have been investigated for OPV application.

	Name and chemical structure	HOMO/LUMO (eV)
<b>Acceptors</b>	Fullerene (C <sub>60</sub> ) 	-5.60/-3.98 [36]
	[6,6]-phenyl-C <sub>61</sub> butyric acid methyl ester (PC <sub>61</sub> BM) 	-6.2/-3.8 [37]
	[6,6]-phenyl-C <sub>70</sub> butyric acid methyl ester (PC <sub>70</sub> BM) 	-6.1/-4.3 [38]
	Single-walled carbon nanotubes (SWCNT) 	-5.05/-4.95 [39]

	<p>5,5'-[(9,9-Dioctyl-9H-fluorene-2,7-diyl)bis(2,1,3-benzothiadiazole-7,4-diylmethylidene)]bis[3-ethyl-2-thioxo-4-thiazolidinone] (FBR)</p> 	<p>-5.70/-3.57 [35]</p>
	<p>Multi-walled carbon nanotubes (MWCNT)</p> 	<p>(3.72)* [40]</p>
	<p>Poly[2-methoxy-5-(2'-ethylhexyloxy)-1,4-phenylene vinylene] (MEH-PPV)</p> 	<p>-5.30/-3.0 [41]</p>
<p><b>Donors</b></p>	<p>Poly (3-hexylthiophene) (P3HT)</p> 	<p>-4.65/-2.13 [42]</p>

	<p>Poly(3-hexylselenophene) (P3HS)</p> 	<p>-4.81/-3.2 [27]</p>
	<p>Poly[2,6-(4,4-bis-(2-ethylhexyl)-4H-cyclopenta [2,1-b;3,4-b']dithiophene)-alt-4,7(2,1,3-benzothiadiazole)] (PCPDTBT)</p> 	<p>-5.02/-3.55 [27]</p>
	<p>Metal-free phthalocyanine (H<sub>2</sub>Pc)</p> 	<p>-7.12/-2.57 [43]</p>
	<p>Copper phthalocyanine (CuPc)</p> 	<p>-4.986/-2.222 [44]</p>

	Metal free porphyrin (H <sub>2</sub> P) 	-7.3/-1.9 [45]
	Manganese phthalocyanine (MnPc) 	-4.468/-4.112 [46]
	Zinc phthalocyanine (ZnPc) 	-5.330/-3.135 [47]

*\*The bandgap of MWCNT indicated instead of HOMO/LUMO energy levels.*

#### 1.1.4. The formation of Excitons

Contrary to the conventional inorganic semiconductors, where upon absorption of photons, free charges; namely, free electrons and holes, are immediately generated; organic material generates neutral mobile excited states known as excitons. The generated excitons diffuse to the D-A interface as shown on Figure 4, where they are separated into free charges. However, the free charges generation efficiency is dependent on overcoming the weak intermolecular forces that localizes the exciton formed [15]; therefore materials with different electron affinities are

used where one with high electron affinity attract electrons; whilst the other with small ionization potential attract holes [48].

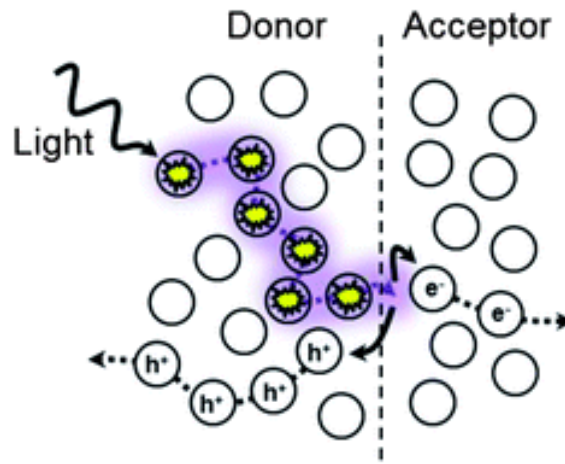


Figure 4. Schematic showing the formation of excitons after absorbing photons [49].

#### 1.1.5. Exciton diffusion length

Exciton diffusion length is a physical quantity that describes the length in which an exciton have to diffuse relative to its lifetime, given to be  $L_D = (D\tau)^{1/2}$ , with  $D$  as diffusion length and  $\tau$  as exciton lifetime [50]. The diffusion length of conjugated polymers range between 4 and 23 nm [51, 52]. On the other hand, the diffusion length of macrocyclic molecules in bilayer assembled active layer consisting of fullerene,  $C_{60}$  as acceptor and phthalocyanines (pcs) as the donor, ranges between 1 and 11 nm; free base phthalocyanine ( $H_2Pc$ ) macrocyclic has the largest  $L_D$  [53]. However, the bilayer configuration (also known as planar heterojunction system) have limited charge separation thus less free charges generated to contribute to the cell current, resulting in low efficiencies are reported for this type of configuration [27]. Although the photon absorption length is  $\sim 100$  nm, the exciton diffusion length remains small [15]. Therefore, the photon have to be absorbed near the D-A interface to ensure efficient charge separation [48], which is not the case in planar heterojunction systems since most of free charges recombine and energy released as heat [14].

The BHJ configuration (also known to have interpenetrating networks) have proven to be ideal for an effective dissociation and transfer of charge because these configurations have an area of

A-D interfaces that spread across the active layer which in form reduces the excitons' minimum path length to diffuse in order to reach the A-D interface [49]; this significantly decreases recombination processes and increases the generation of free charge [20]. Therefore, when considering assembling an active layer, the diffusion length of both the photon and the exciton should be considered.

### 1.1.6. Exciton separation

The exciton, also known as hole-electron pairs, are metastable, the pairs remain coulombically attracted even after partially separating into free charges at the heterojunction (A-D interface). Therefore, for the charges to be completely separated, electric field is required [54]. This is achieved by varying the work function of the anode and cathode materials [15]. Thereafter, the free charges will migrate until they reach respective materials (Figure 5). Brabec et al. [55] varied the work function of the electrodes for Poly[2-methoxy-5-(3',7'-dimethyloctyloxy)-1,4-phenylenevinylene] (MDMO-PPV): fullerene derivatives BHJ cell to determine its influence on the open-circuit voltage ( $V_{oc}$ ) thus the efficiency of the cell and concluded that the internal electric field does not have an effect on the  $V_{oc}$  but it is dependent on overlap of the energy levels of the organic material in the active layer. Despite the influence of electric dipole at the D-A interface that is responsible for the partial dissociation of excitons, the offset energy (depicted as  $E_a$  in Figure 5) known as the energy between the LUMO-LUMO and HOMO-HOMO energy levels of the donor and acceptor material (Figure 5), that is  $\Delta E_{HOMO}$  or  $\Delta E_{LUMO}$  respectively; have to be greater than the binding energy  $\Delta E_{B(D,A)}$ , to ensure an effective CT [56]. Upon charge dissociation at the heterojunction, exciton excess energy is given as  $E^* = \Delta E_{LUMO} - E_{B,D}$  and excess energy in the acceptor material is given as  $E^* = \Delta E_{HOMO} - E_{B,A}$ , which is converted to kinetic energy for holes and electrons respectively [57]. Therefore, an efficient complete dissociation and collection of charges are subject to the internal electric field strength.



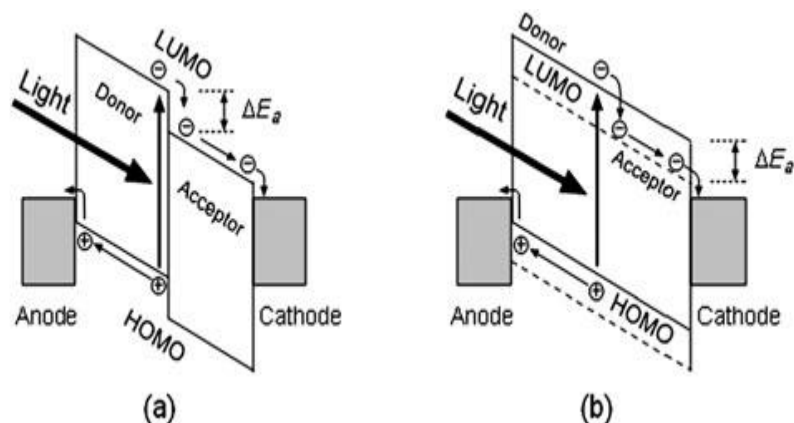


Figure 5. Diagram showing the processes that occurs in (a) planar/or bilayer heterojunction (PHJ), and (b) bulk heterojunction (BHJ) systems [14]. (b) The dashed lines show both the HOMO and LUMO energy levels.

## 1.2. Materials- Donors and acceptor used in this study:

### 1.2.1. Acceptor: MWCNT

Carbon nanotubes (CNTs) are carbon allotropes that have tube-like shape that consist of graphene sheets with varying outer diameter ranging from 3 nm to 30 nm [58]. CNTs have been widely investigated since their discovery, in 1991 [59]. This is due to their remarkable properties such as large surface area, high electrical conductivity, and exceptional mechanical strength [60]. Their application includes photocatalytic reduction of CO<sub>2</sub> to hydrocarbons fuels, artificial photosynthesis, organic photovoltaic cells, optoelectronics and sensing devices [61]. There are two types of CNTs namely, single-walled carbon nanotubes (SWCNTs) and multi-walled carbon nanotubes (MWCNTs) [58]. SWCNTs are made up of single graphene layer whilst MWCNTs are made of multiple graphene layers (Figure 6).

MWCNTs are preferred over SWCNTs because the use of catalyst not only reduces the purity of the product but also complicates the synthetic process [58]. Whereas MWCNTs have low synthesis cost thus making high purity materials readily available [62]. Xiao et al. [63] used poly(3,4-ethylenedioxythiophene) (PEDOT)/MWCNT films as an alternative counter electrodes (CE) in the fabrication of dye-sensitized solar cells (DSCs) and reported an exceptional 7.03% power conversion, an increase from 5.88% when using Pt CE, this is attributed to the nanotubes' large charge carrier. Similarly, the P3HT:PCBM BHJ active layer was doped with functionalized

MWCNT showed an improvement in the efficiency of the cell attributed to MWCNT's high exciton separation and transport of charge [62]. Lastly, the MWCNT were employed for IR detection due to its band gap (given to be 3.72 eV [40], Figure 9).

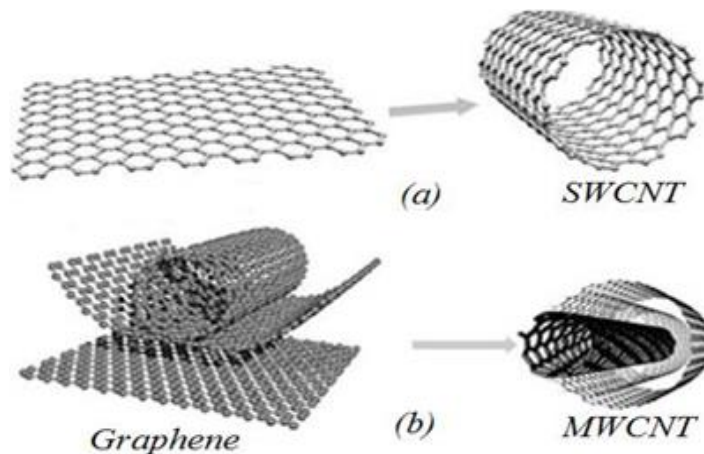


Figure 6. Molecular structure of (a) Single-walled carbon nanotube (SWCNT), (b) Multi-walled carbon nanotube (MWCNT) [64].

### 1.2.2. Donors: Phthalocyanines

Phthalocyanines (pcs) are comprised of benzo-fused pyrroles joined by nitrogen (N) atoms to make  $18\pi$  electrons ( $e^-$ ) ( $18\pi e^-$ ) delocalized flat macrocyclic compounds [65, 66]. These macrocyclic dyes were discovered as a result of an accidental finding by William Henry Perkin when investigating the treatment for malaria [67]. They also have similar structural composition as the naturally occurring molecules such as chlorophyll and haemoglobin [68]. The empty centre in the macrocyclic compounds can be filled by a metal, mostly transition metals (TMs), or utilized as is [65]. For instance when the centre is not filled with any TMs then a two-fold symmetrical compound known as metal-free phthalocyanine ( $H_2Pc$ ) [65] is obtained as depicted Figure 7 (a), with the bandgap ( $E_{gap}$ ) given to be 4.55 eV (Figure 9), where HOMO= -7.122 eV and LUMO=-2.565 eV [43].

The delocalization of  $18\pi e^-$  in pcs [66] is attributed to their exceptional properties such as high chemical and thermal stability, quality crystallisation films, outstanding charge carrier mobilities and tunability of the chemical properties [13]. Hence they find wide application in OPV (as p-type

semiconductors), gas sensors, cancer therapy, organic light emitting devices and magnetic switches [69]. Apart from the properties indicated above, pcs also absorbs intensely in the region 600-800 nm of the visible range where there is a high solar photon flux, making them good p-type semiconductors and this explains their utilization in OPV [13].

The properties of pcs can be tuned by adding substituents, or central metals, mostly transition metals (TM) [70, 71]. The first metallated phthalocyanine, now known as copper phthalocyanine (CuPc), was reported in 1927 by de Diesbach and von der Weid [68]. Since then, various transition metals have been inserted into pcs, yielding metal phthalocyanines (MPcs) [71]. For example, when pc is complexed with Zn to make zinc phthalocyanine (ZnPc) then fabricate ZnPc:C<sub>60</sub> PHJ OPV cell, a notable increase power conversion ranging between 0.84 and 4% [13, 53] were observed in comparison to 0.03% of H<sub>2</sub>Pc:C<sub>60</sub> PHJ OPV cell [13, 72]. This is attributed to the metal's contribution to electron density of these macrocyclic compounds [73].

Like other p-type semiconductors, the bandgaps (LUMO-HOMO energy levels) of MPcs are considered in the fabrication of OPVs solar cells where smaller compounds with smaller bandgaps are preferred. Although the bandgap of MnPc (Figure 7 (b)) is  $E_{\text{gap}} = 0.356$  eV with HOMO = -4.468 eV and LUMO = -4.112 eV [46] (Figure 9) is much smaller than that of ZnPc ( $E_{\text{gap}} = 2.195$  eV [47]), the compound has not been intensely studied compared to other transition metal counterparts such as Fe, Co, Ni, Zn and Cu; which forms a basis for current study.

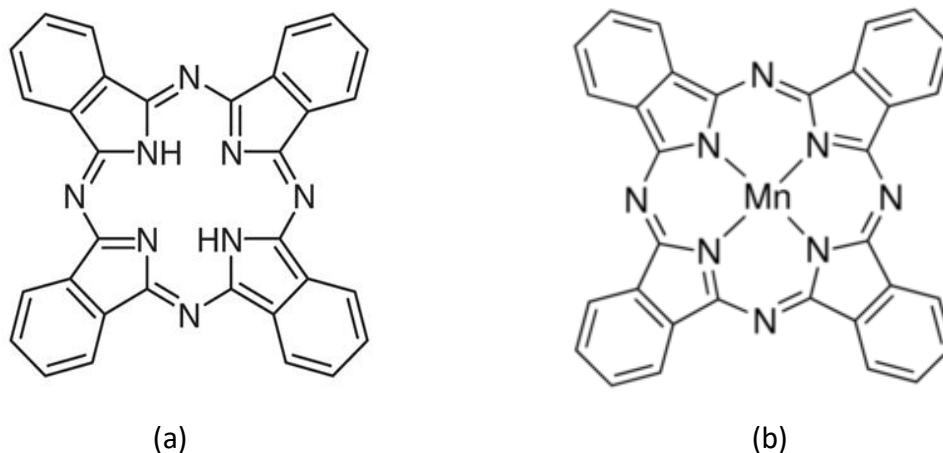


Figure 7. Molecular structure of metal-free phthalocyanine (H<sub>2</sub>Pc) (a) and Manganese II phthalocyanine (MnPc) (b).

### 1.2.3. Conjugated conducting polymer: PCPDTBT

Conjugated polymers consist of alternating single-double bond backbone chain where the  $\pi$ -electrons are delocalized throughout the system [74, 75]. Although the electrons are delocalized in these systems, they are not necessarily conductive because the carbon chains are covalently bonded; hence interchanging donating or accepting units such as benzene, pyrrole, alkoxy, amines, thienopyrazine, thiophene, thiazole, trifluoromethyl are introduced [27]. The delocalized electron network is responsible for exceptional electrical, optical, thermal, and mechanical properties of these conducting polymers. This accounts for their wide employment in neurological sensing, thermoelectric harvesters [76], electrochromic displays and agricultural sensing and organic photovoltaic solar cells to name a few [77].

The use of conducting conjugated polymers in the fabrication of OPV solar cells has received great attention since the discovery of charge transfer between  $C_{60}$  and MEH-PPV [18]. Particularly, poly-phenylene vinylene (PPV) and poly-thiophenes [78]. Poly (3-hexylthiophene) (P3HT) being the most used polymer in OPVs and had the highest reported PCE for BHJ solar cell [79]. However, despite P3HT based BHJs outstanding success, its LUMO energy level is high and affect how it overlaps with the energy levels of the acceptor, specifically PCBM, yielding inefficient charge transfer thus loss of  $V_{oc}$  [35]. Hence, alternative conjugated polymers with lower band gap have been considered. This includes Poly(3-hexylselenophene(P3HS), Poly5,7-bis(3,4-diethylhexyloxy-2-thienyl)-2,3-diphenyl-thieno[3,4-b]pyrazine(PBEHTT), Poly5,7-di(2-thienyl)-2,3-bis(3,5-diethylhexyloxyphenyl)-thieno[3,4-b]pyrazine(PTBEHT) and Poly[2,6-(4,4-bis(2-ethylhexyl)-4H-cyclopenta [2,1-b;3,4-b']dithiophene)-alt-4,7(2,1,3-benzothiadiazole)](PCPDTBT) [27]. Thus, for this research PCPDTBT was considered.

PCPDTBT has fused alternating donor and acceptor units of two thiophene rings and benzothiadiazole as shown in Figure 8 (a) [27]. These alternating units are responsible for lowering the LUMO and HOMO energy levels of the conjugated polymer thus decreasing the band gap ( $E_{gap} = 1.47$  eV) [80]. Hence the LUMO and HOMO of PCPDTBT is lowered to -3.55 and -5.02 eV [27] (figure 9) respectively compared to -2.13 and -4.65 eV of P3HT (Figure 8 (b)) [42]. A small

bandgap in PCPDTBT allows it to absorb longer wavelength, accumulating ~ 64% of the solar spectrum [32] with reported PCPDTBT: PC<sub>71</sub>BM based BHJ cell efficiencies ranging between 5.2-5.8% [81]. In addition, Albrecht et al. [82] reported a remarkable 7% PCE for PCPDTBT based BHJ solar cell where decreased charge recombination rate is obtainable.

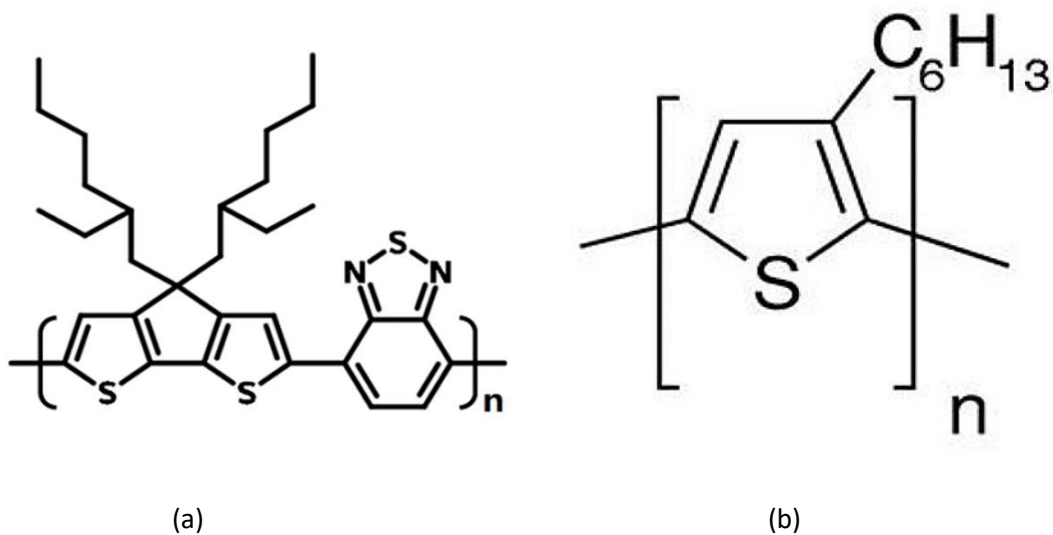


Figure 8. Molecular structure of PCPDTBT (a) and P3HT (b).

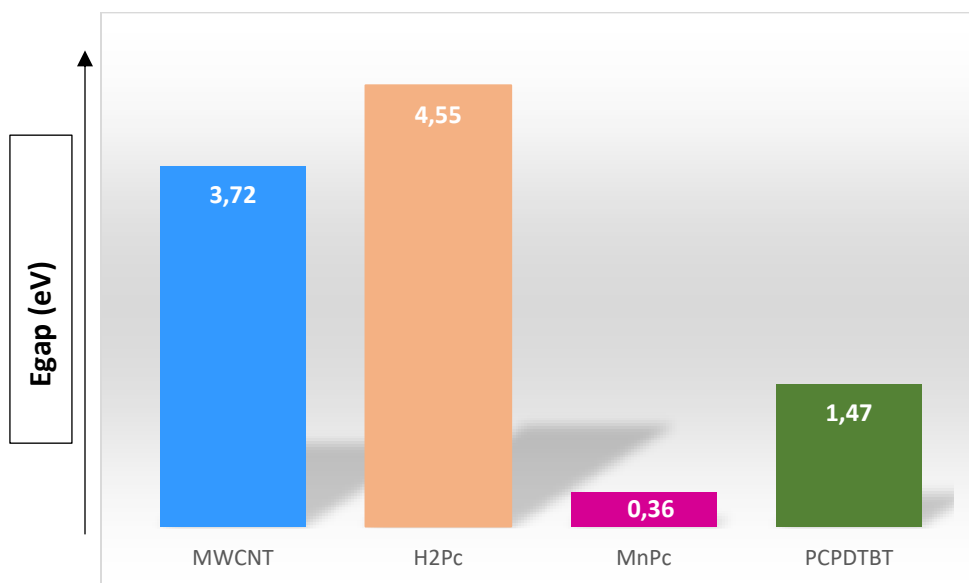


Figure 9. A plot of energy band gaps of the acceptor and donor materials considered for this project.

# Chapter 2 Methodology

## 2. Experimental work

### 2.1. Absorbance and Fluorescence measurements

The absorption titration measurements were carried out on CARY 100 Bio UV-Visible double beam spectrophotometer. Baseline corrections recorded using a pair of 10 mm quartz cuvettes in the 200-800 nm range using chlorobenzene (CBZ) solvent (Sigma-Aldrich, ACS grade solvent  $\geq 99.5\%$ ) as a blank. The double-beam instrument offers data that is more reliable since the results can be obtained if the experimental method is duplicated. The instrument does this by instantaneously rectifying the beam intensity depletion as it goes past the blank and analyte material [83].

The fluorescence titration measurements were conducted on Horiba Jobin Yvon FluoroMax-4 spectrofluorometer, with the slit width set to 5 nm and xenon as a light source. MWCNT (0.05 mg/mL) was titrated against variable concentrations of donors from 0 to  $70 \times 10^{-5}$  M for H<sub>2</sub>Pc, 0 to  $5 \times 10^{-5}$  M for MnPc and 0 to  $9 \times 10^{-7}$  M for PCPDTBT. Absorption spectra were further recorded to determine the excitation wavelengths. Thereafter, emission spectra of MWCNT: Donor (H<sub>2</sub>Pc, MnPc and PCPDTBT) solutions were recorded immediately after measuring absorption spectra, minus the intensity due to CBZ solvent. The MWCNT: H<sub>2</sub>Pc solutions were excited at 518 and 650 nm, MWCNT: MnPc solutions were excited at 503 and 650 nm; while MWCNT: PCPDTBT solutions were excited at 370, and 650 nm. H<sub>2</sub>Pc (98% purity), MnPc and PCPDTBT were obtained from Sigma Aldrich. MWCNT (98% carbon purity) was obtained from Sabinano, SA. These compounds were used without any further purification.

The Benesi-Hilderbrand (BH) equation was employed for the calculation of the binding constant, K. A 1:1 stoichiometric ratio was assumed, and the equation is given as.

$$\frac{A_0}{A_0 - A} = \frac{\epsilon_{CNT}}{\epsilon_{CNT} - \epsilon_{D-CNT}} + \left( \frac{\epsilon_{CNT}}{\epsilon_{CNT} - \epsilon_{D-CNT}} \right) \times \left( \frac{1}{K[D]} \right) \quad (1) [84]$$

Where  $A_0$  is the initial absorbance of the donor free solution, while  $A$  is the absorbance of the MWCNT-Donor (D) solution. Furthermore,  $D$  is the concentration of the donor materials;  $K$  is the binding constant and molar extinction coefficient of MWCNT, and MWCNT-Donor solution represented by  $\epsilon_{\text{CNT}}$  and  $\epsilon_{\text{D-CNT}}$  respectively. The same equation as (1) was employed for calculating the binding constant,  $K$ , from the emission measurements where the  $A_0$  is replaced with  $I_0$  (initial intensity of the donor free solution) and  $A$  with  $I$  (intensity of the MWCNT-Donor (D) solution).

## 2.2. *Electrochemistry measurements*

Cyclic voltammetry (CV) is a common method used to evaluate the materials redox steps [85] and allows for the observation of a wider potential window. On the other hand, differential pulse voltammetry (DPV) is a highly sensitive voltammetric technique that enables the detection of very small quantities of electroactive organic materials [86]. Hence, both voltammetric methods were employed to understand the redox behaviour of the donors and acceptor along with their interaction via titration.

Voltammetric measurements were carried out at RT on Metrohm Autolab Type III (PGSTAT100, AUT71886) controlled via Nova 2.0 electrochemistry software. The three-electrode cell setup (Figure 10) was employed with glassy carbon (GC) working electrode, silver (Ag) wire pseudo reference electrode, platinum (Pt) wire counter electrode, 0.01M tetrabutylammonium hexafluorophosphate (TBA-PF<sub>6</sub>) was used as a supporting electrolyte (SE), and ortho dichlorobenzene (oDCB) (Sigma-Aldrich, HPLC grade solvent 99%) as a solvent. Fc/Fc<sup>+</sup> is used as internal standard and measurements were taken by adding Fc at the end of every experiment.

The solutions were purged for a minimum of 30 minutes with nitrogen (N<sub>2</sub>) gas before running each experiment, for 5 minutes prior to each potential interval while titrating with MWCNT the donor solutions were purged for 15 minutes after each addition. Similarly, GC and Ag wire electrodes were polished between every potential window while measuring. Blank experiment with SE and solvent was conducted to make sure that there no interference from the solvent in the potential window used.

The CVs and DPVs were recorded at scan rates of 0.05 V/s and 0.1 V/s, and 5 mV and 10 mV pulse amplitudes respectfully. Thereafter, DPV titrations were carried out at 10 mV modulation amplitude. The donor (H<sub>2</sub>Pc, MnPc and PCPDTBT) solutions were titrated with increasing concentrations of MWCNT (0 – 4 mL aliquots of 0.05 mg/mL).

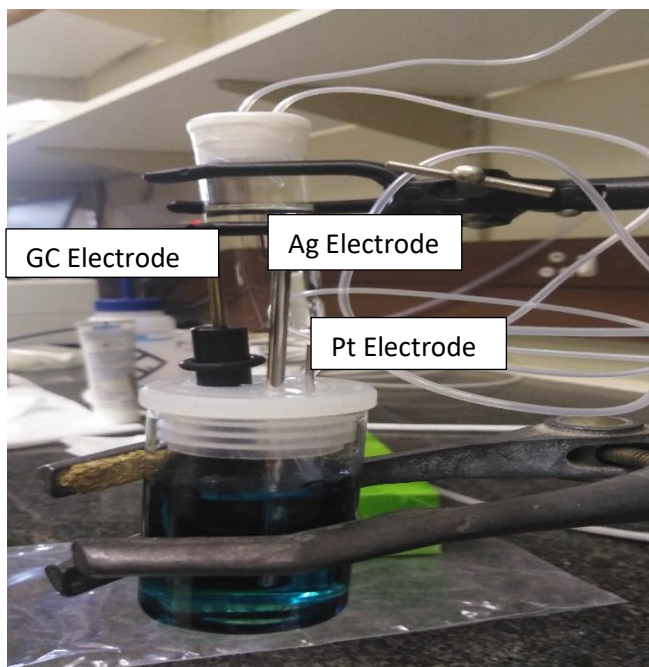


Figure 10. A three-electrode cell setup.

### 2.3. Fluorescence quantum yield measurements

The fluorescence quantum yield ( $\Phi_F$ ) measurements were conducted following the matched method by Williams *et al.* [87] measured on Horiba Jobin Yvon FluoroMax-4 spectrofluorometer, and Specord 200 Plus (double beam instrument) spectrophotometer using zinc phthalocyanine (ZnPc  $\Phi_F = 0.30$ ) in 1-chloronaphthalene excited at 625nm [88] for phthalocyanine quantum yield measurements and Rhodamine 6G (Rh-6G) used as a reference standard with  $\Phi_F = 0.95$  in ethanol as solvent, excited at 559 nm [88] for the conjugated polymer quantum yield measurements. The fluorescence quantum yields were calculated using the equation shown below,

$$\Phi_{F(A)} = \Phi_{F(ST)} \left( \frac{Grad_A}{Grad_{Std}} \right) \left( \frac{\eta_A^2}{\eta_{Std}^2} \right) \quad (2)$$



with ST and A as standard and analyte, respectively. Similarly,  $\Phi_F$  as the fluorescence quantum yield, *Grad* as gradient of the linear plot of fluorescence intensity against absorbance and  $\eta$  as the solvent refractive index measured [89]. Chlorobenzene (CBZ) was used as a solvent instead of 1-chloronaphthalene since CBZ's dielectric constant is similar to that of 1-chloronaphthalene. On the other hand, chloroform was used instead of EtOH because it readily available dissolves Rh-6G.

#### 2.4. *Transmission Electron Microscopy (TEM) measurements*

Transmission electron microscope (TEM) is a microscopic technique that uses high voltage electrons instead of a light source emitted from the electron gun (Figure 11), onto a sample substrate. The utilization of the small wavelength light source [90] allows for high resolution image of the structural composition of the sample analysed. The electron beams are focused using the electromagnetic lenses as they pass through a vacuumed tube (Figure 11) then transmitted through a film substrate; however, the transmittance of the beam is dependent on the thickness of the deposited sample on the film [91]. Thereafter, the refocused (Figure 11) and the composition of the sample is observed.

The TEM measurements were carried out on FEGTEM Jeol 2100 with an emission transmission field of 200 kV. The blends of MWCNT-MPc (M=H, and Mn) /PCPDTBT were drop coated on a carbon coated copper grids, dried under an IR lamp for 15 minutes then left to complete drying overnight at RT. Thereafter, the structural arrangements of the complexes formed were investigated.

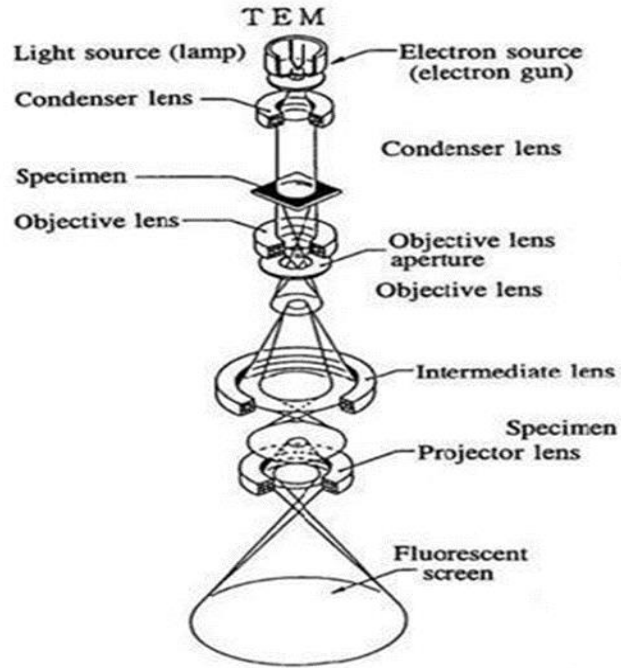


Figure 11. Transmission electron microscope (TEM) diagram [90].

## Chapter 3 Results and discussion

### 3. Spectrophotometric, voltammetric and TEM measurements

#### 3.1. *Uv-vis spectroscopy and molar extinction coefficients of the pristine compounds.*

The Uv-vis spectra of phthalocyanines (pcs) are characterized by Soret- (also known as B)- and Q-bands, where the transitions responsible for these bands are accredited to  $S_0 \rightarrow S_2$  and  $S_0 \rightarrow S_1$  respectively. The UV-visible spectra of free-base phthalocyanines ( $H_2Pc$ ) as a function of concentration in chlorobenzene as shown in Figure 12, shows the characteristic shoulders observed at 601 nm and 635 nm then a split Q-band identified as  $Q_x$ - and  $Q_y$ -band observed at 661 nm and 697 nm. This split of Q-bands is attributed to the  $D_{2h}$  symmetry [92]. The transitions characteristic of the split Q-band is the  $Q_x$  and  $Q_y$  states namely (0,0) and (0,1) vibrational states while shoulders arise as a results of vibronic transitions within  $Q_x$  and  $Q_y$  states [93, 94].

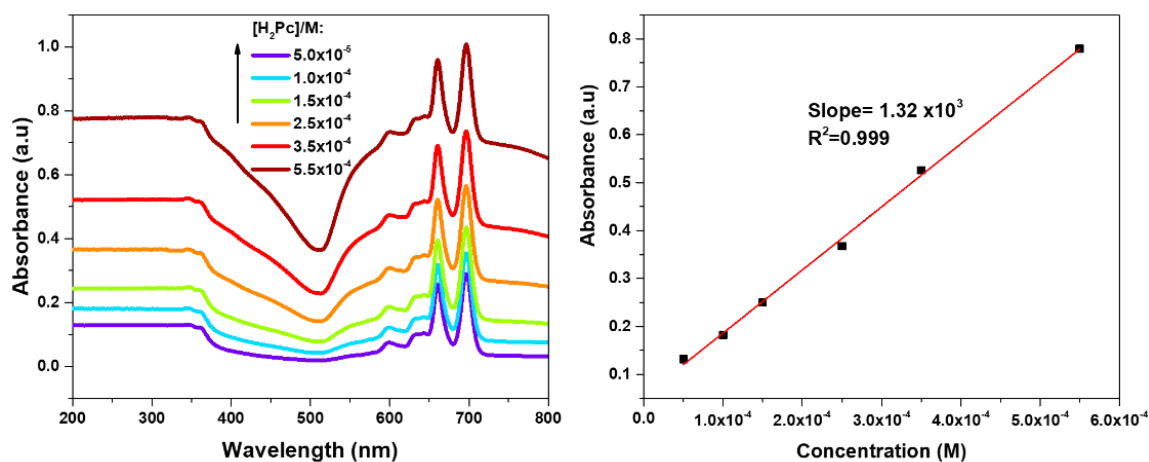


Figure 12. Left: Uv-vis absorption spectrum of varying concentrations  $H_2Pc$  ( $0.5$  to  $5.5 \times 10^{-4}$  M; indicated by traces purple to dark red) in CBZ; Right: Absorbance against concentration of  $H_2Pc$  for the calculation of molar extinction coefficient at 347 nm.

Figure 13 shows that manganese phthalocyanine (MnPc) has an absorptive band in the Soret region at 359 nm characterized by  $S_0 \rightarrow S_2$  electronic transition. Unlike the  $H_2Pc$  the absorption spectra of MnPc shows an absorption peak appearing at 522 nm arises as result of CT from the electron rich ring to the electron-deficient metal-ion, followed by vibronic shoulder at 653 nm and an intense Q absorption band at 723 nm.

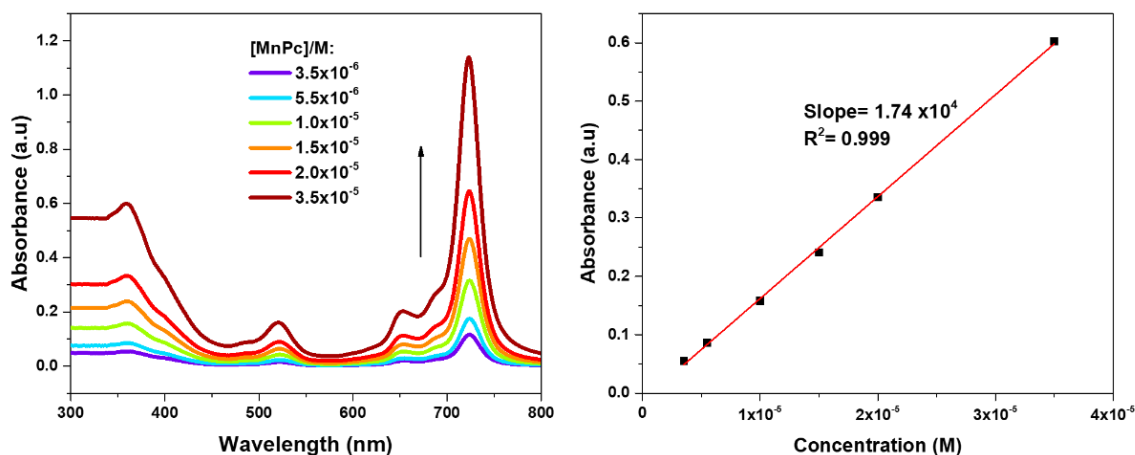


Figure 13. Left: *Uv-vis absorption spectrum of varying concentrations MnPc ( $0.35$  to  $3.5 \times 10^{-5}$  M, indicated by traces purple to dark red) in CBZ; Right: Absorbance against concentration of MnPc for the calculation of molar extinction coefficient at 359 nm.*

The absorption spectra of PCPDTBT is identifiable by two bands (Figure 14), absorptive band at the higher wavelength observed at 410 nm arises as a result of  $S_0 \rightarrow S_n$  with  $n$  being the number of allowed states by permitted  $\pi-\pi^*$  interchain transitions while the redshifted broad peak at 712 nm is accredited to  $S_0 \rightarrow S_1$  [95]. PCPDTBT absorbs a broader section of the UV-vis spectrum compared to its counterpart P3HT that only absorbs at the smaller wavelengths, in the region 300-550 nm [96].

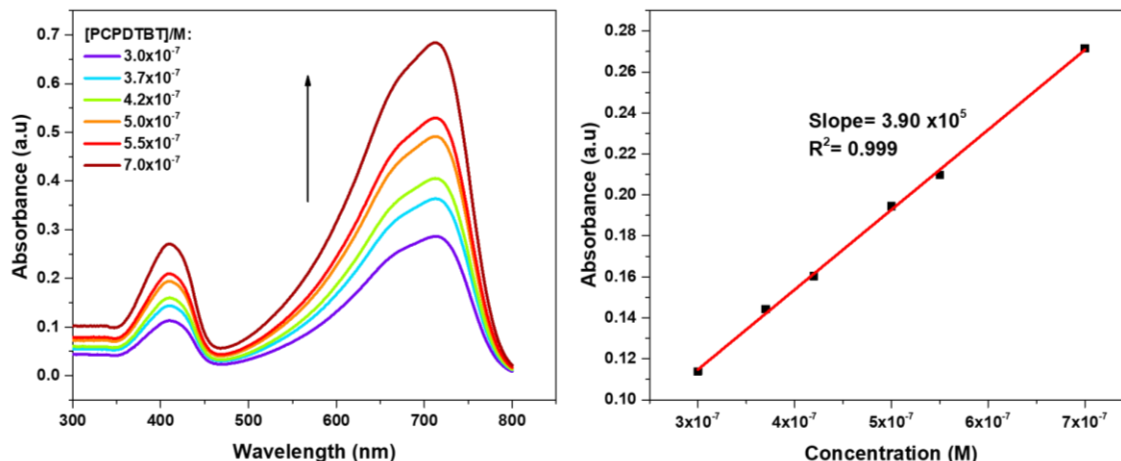


Figure 14. Left: Uv-vis absorption spectrum of varying concentrations PCPDTBT ( $3.0$  to  $7.0 \times 10^{-7}$  M; indicated by traces purple to dark red) in CBZ; Right: Absorbance against concentration of PCPDTBT for the calculation of molar extinction coefficient at  $410$  nm.

Figure 15 indicates that the MWCNT do not show any absorptive peak in the UV-visible region. On the contrary, Cheng *et al.* [97] reported an absorption spectrum showing a peak in the range  $240$ - $265$  nm recorded in water, the absence of peaks in the absorption spectrum of MWCNT in this project can be attributed to the UV solvent cut-off with that of water being at  $190$  nm whereas that of CBZ is at  $287$  nm. Furthermore, MWCNT are suspensions in the solvent used, hence, the Figure 15 typically shows structureless and high absorbance values.

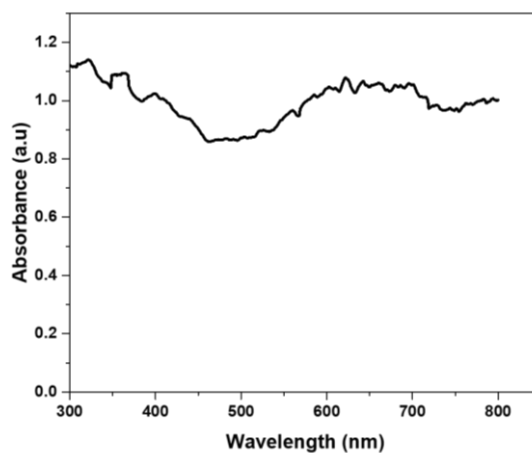


Figure 15. The UV-vis absorption spectrum of  $0.1$  mg/mL MWCNT recorded in CBZ.

The Lambert-Beer law states that the proportionality between absorbance of a solution and its concentration is given by the equation  $A = -\log(I/I_0) = \epsilon_0 LC$ ; where the  $I/I_0$  is the initial and final light

intensity of the solution respectively,  $\epsilon_0$  is the molar extinction coefficient,  $L$  is the path length of the cuvette and  $c$  is the concentration of the analyte solution. This was employed to determine the  $\epsilon_0$  of 3 donors using the absorbance against concentration plot, the gradient of the plots provides the molar extinction coefficient.

*Table 2. Molar extinction coefficients ( $\epsilon_0$ ) of H<sub>2</sub>Pc, MnPc and PCPDTBT calculated at 679 nm, 724 nm, and 712 nm respectively in CBZ.*

<b>Compounds</b>	<b><math>\epsilon_0</math> (M<sup>-1</sup>cm<sup>-1</sup>)</b>
<b>H<sub>2</sub>Pc</b>	1.40 x 10 <sup>3</sup>
<b>MnPc</b>	3.26 x 10 <sup>4</sup>
<b>PCPDTBT</b>	9.84 x 10 <sup>5</sup>

The molar extinction coefficients ( $\epsilon_0$ ) shown in Table 2 were only calculated for intensive transitions, that is the Q-bands for phthalocyanines (pcs) because the Q bands are usually disconnected from the vibronic transitions [98] and the broad redshifted band for PCPDTBT. The molar extinction coefficient of MnPc is larger than that of the free-base phthalocyanine indicating that the material strongly absorbs at lower energies [99]. In contrast, Taniguchi and Lindsey [88] reported the  $\epsilon_0$  to be 1.62x10<sup>5</sup> M<sup>-1</sup>cm<sup>-1</sup> for H<sub>2</sub>Pc in chloronaphthalene whereas that of MnPc is smaller with  $\epsilon_0$  given to be 4.68x10<sup>3</sup> M<sup>-1</sup>cm<sup>-1</sup> in chlorobenzene [100]. Even though the molar extinction coefficients of phthalocyanines are lower, there is evidence that all donors generate photocurrent. On the other hand, the PCPDTBT show exceptionally high extinction value, greatly absorbs light at 712 nm in a similar range as P3HT, with  $\epsilon_0$  given to be 1.00 x10<sup>5</sup> M<sup>-1</sup>cm<sup>-1</sup> [31]. PCPDTBT thus substantially contributes to the photocurrent generation in OPVs [82, 101].

### *3.2. Fluorescence spectroscopy and Quantum Yields*

The fluorescence spectrum of H<sub>2</sub>Pc shows a single intense emission peak observed at 696 nm and three shoulders one at the lower wavelength and two others on the redshifted region, appearing at 661 nm, 730 nm, and 775 nm respectively (Figure 16).

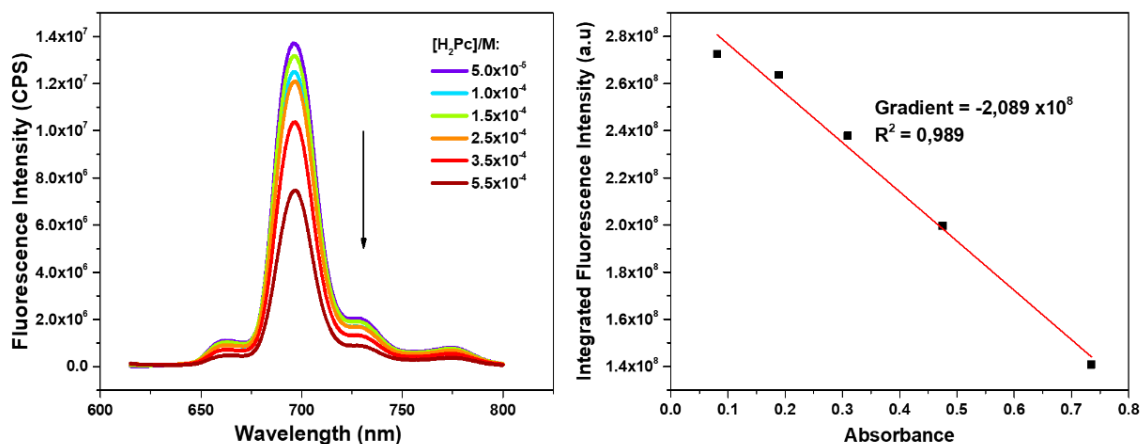


Figure 16. Left: Fluorescence spectrum of H<sub>2</sub>Pc (0.5 to 5.5 × 10<sup>-4</sup> M; indicated by traces purple to dark red) in CBZ; Right: Linear plot of absorbance against integrated fluorescence of H<sub>2</sub>Pc in CBZ to calculate fluorescence quantum yield excited at 600 nm.

The transitions responsible for intense emission peak at 696 nm allocated to the (0,0) vibrational transition while the shoulder appearing at 730 nm is assigned at (0,1) transition [93]. The transitions responsible for the shoulder appearing at 775 nm are unclear with the least likely being (0,2) and the more likely one would be either (0,1) or (0,0).

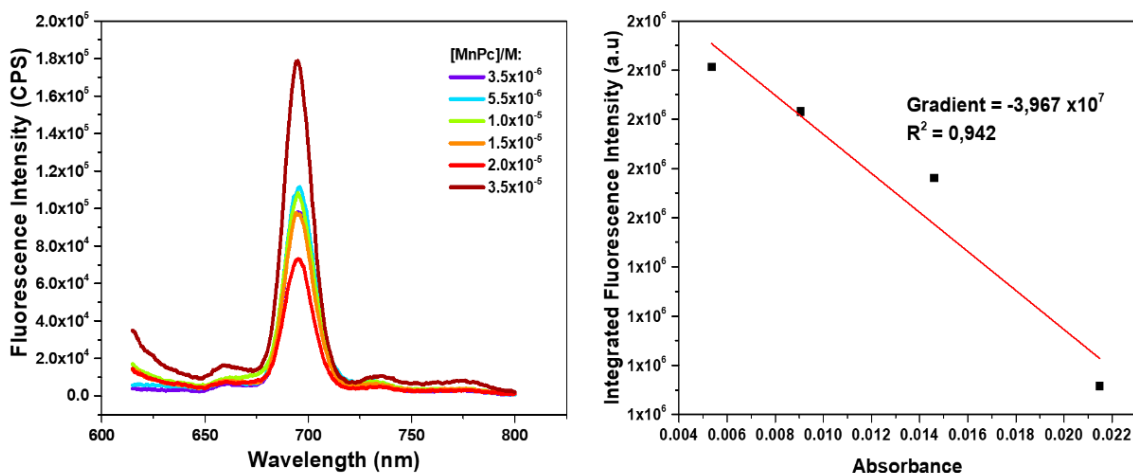


Figure 17. Left: Fluorescence spectrum of MnPc (0.35 to 3.5 × 10<sup>-5</sup> M; indicated by traces purple to dark red) in CBZ; Right: Linear plot of absorbance against integrated fluorescence of MnPc in CBZ to calculate fluorescence quantum yield excited at 600 nm.

Furthermore, the emission spectra of increasing concentration of MnPc shows an intense peak at 695 nm, and shoulders at 659 nm, 735 nm, and 777 nm (Figure 17). The stronger band at 695

nm arises due to (0,0) transition while shoulder at 659 nm occurs because of movement from the high vibrational state to the ground state  $S_1 \rightarrow S_0$ .

Lastly, the fluorescence spectrum of PCPDTBT excited at 624 nm (Figure 18), shows a single emission peak at 766 nm illustrated by (2,1) vibrational transition [95].

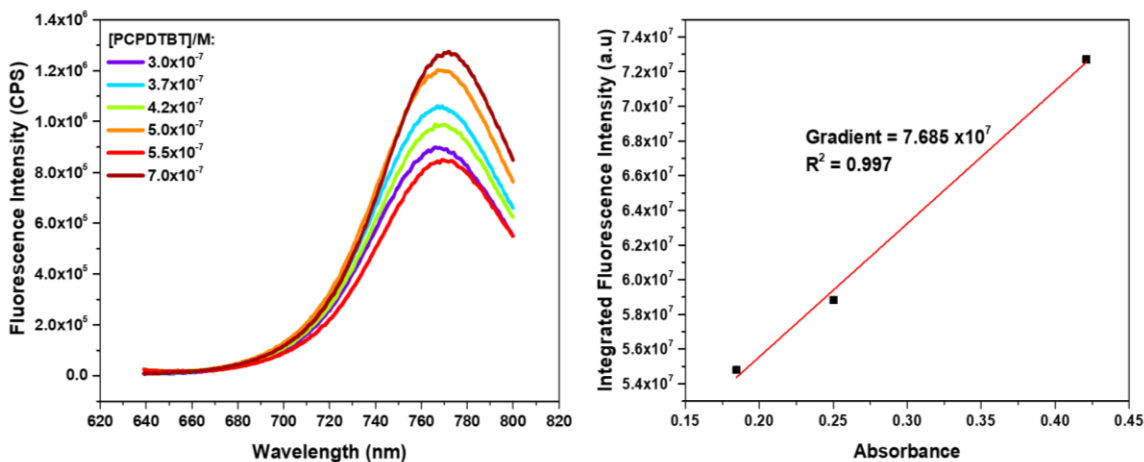


Figure 18. Left: fluorescence spectrum of PCPDTBT ( $3.0$  to  $7.0 \times 10^{-7} M$ ; indicated by traces purple to dark red) in CBZ; Right: Linear plot of absorbance against integrated fluorescence of PCPDTBT in CBZ to calculate fluorescence quantum yield excited at 624 nm.

The fluorescence quantum yields ( $\Phi_F$ ) were calculated from linear plots of integrated fluorescence intensity against absorbance (Figure 16 and 17) from varying concentrations of  $H_2Pc$ , and  $MnPc$  respectively, using uv-vis and fluorescence spectra with  $ZnPc$  used as a standard (with  $\Phi_F=0.30$  in 1-chloronaphthalene at 625 nm). Similarly, for PCPDTBT, Rhodamine 6G (Rh-6G) was used as a standard ( $\Phi_F= 0.95$  in EtOH at 559 nm) (Figure 18). The equation used to determine fluorescence quantum yield is equation 2, as discussed in chapter 2.3.



Table 3. The fluorescence quantum yield ( $\Phi_F$ ) of pcs at 600 nm and of PCPDTBT at 624 nm in chlorobenzene (CBZ) and chloroform respectively, measured at RT.

Compounds	$\Phi_F$
<b>H<sub>2</sub>Pc</b>	0.886
<b>MnPc</b>	0.168
<b>ZnPc (Std)</b>	0.30 [88] ( $\lambda_{ex} = 625$ nm)
<b>PCPDTBT</b>	0.833
<b>Rh-6G (Std) in chloroform</b>	0.95 [88] ( $\lambda_{ex} = 559$ nm)

The fluorescence quantum yields ( $\Phi_F$ ) from Table 3 indicate that the Pcs does not efficiently release the excited charge at higher wavelengths. It is notable that the MnPc quantum yields are lower compared to the H<sub>2</sub>Pc, in concurrence with the literature [88, 102] this can be attributed to the central metal being paramagnetic which decreases the  $\Phi_F$  [103]. PCPDTBT on the other hand (Table 3), has larger quantum yield than the other donors, even larger than of P3HT recorded in CBZ reported to be  $0.33 \pm 0.07$  [104] which is expected owing to the polymeric nature of the compound, heavy conjugation and its absorption going well into the visible region (Table 2).

The motive of the present research work is to understand the acceptor-donor interactions between MWCNT and the Pcs / PCPDTBT donors. These compounds are generally hydrophobic and are prone to aggregation. Hence, the study must be done at the concentrations where these compounds do not undergo self-aggregation. Hence, the absorption and emission spectra of the donors were run at varying concentrations as shown in Figures 12, 13 and 14. These figures also show on their right, the plot of absorbance as a function of concentration which yields a straight line. This indicates that under this concentration range, the compounds were monomeric in nature and hence this concentration range was used to study their interactions with MWCNT via titration experiments as discussed *vide infra*.

### 3.3. Spectrophotometric Titrations

UV-vis absorption and fluorescence spectroscopic techniques were employed to determine a plausible interaction between the acceptor and donor materials. The objective is to investigate the changes to the spectral behaviour of the complexes, if formed during the experiments.

#### 3.3.1. $H_2Pc$ -MWCNT titration

The absorption spectral changes upon the addition of increasing concentrations of  $H_2Pc$  to MWCNT is shown in Figure 19. The Q-bands do not provide any evidence of shifting and broadening but simply increase in the absorbance with increase in the concentration of  $H_2Pc$ . However, fluorescence spectra obtained by excitation at 650 nm wavelength (Figure 19: right) show a mild quenching of fluorescence doublet of 689 and 702 nm with increasing  $H_2Pc$  concentration (Figure 19, traces from blue to green) this quenching can be assigned to a charge transfer interaction from  $H_2Pc$  excited states to MWCNT thus the formation of the MWCNT- $H_2Pc$  complex. It is worth mentioning here that in the emission spectra, a decrease in the fluorescence is named as quenching when a molecule is added to an existent system. This feature can also turn around and increase after a particular concentration which is attributed to an interaction happening at a certain concentration after which the emission intensity can increase.

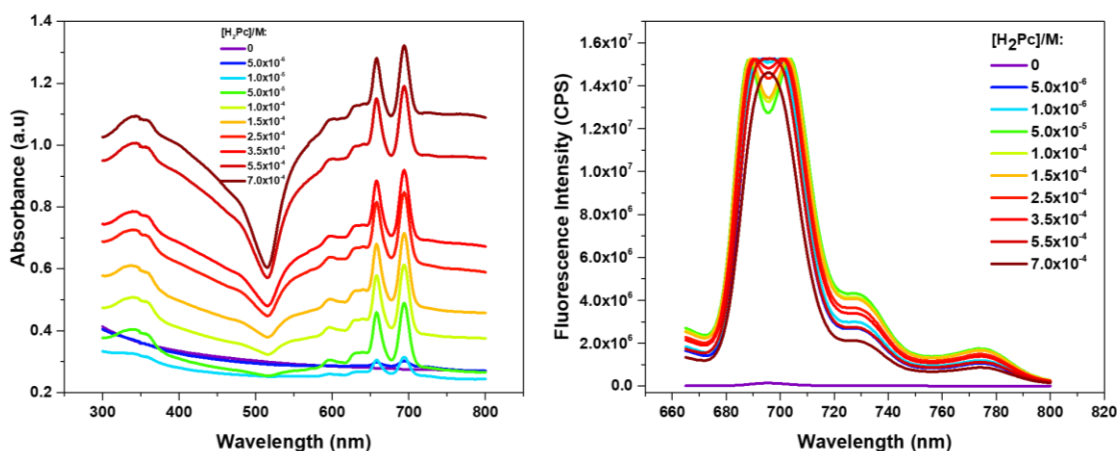


Figure 19. Spectral changes upon the addition of variable concentration of  $H_2Pc$  (0 to  $7 \times 10^{-4} M$ ) to 0.05 mg/mL of MWCNT in CBZ. Left: Absorption Spectrum; Right: Emission Spectrum,  $\lambda_{ex} = 650$  nm.

### 3.3.2. MnPc-MWCNT titration

The absorption spectral changes upon the formation of the MWCNT-MnPc supramolecular complex show increase in the absorbance with increasing concentration of MnPc. However, as can be evidenced from Figure 20, at concentrations to the end of titration (light red traces in Figure 20) a crossover is seen in the traces before there is a further increase in absorbance along with a complimentary broadening of 382 nm Soret band. In the emission spectra in Figure 20 right, a considerable increase in fluorescence along with the broadening and merging of the 734 and 776 nm emission feature in comparison to figure 17 is evidenced. All the above factors indicate a favourable interaction between the MWCNTs and the MnPc, despite an extremely unstable nature of MnPc [98]. Again, worth mentioning here is that during titration, the fluorescence intensity increase, or decrease can be generally attributed to the association between the titrant molecules, which justifies our observation.

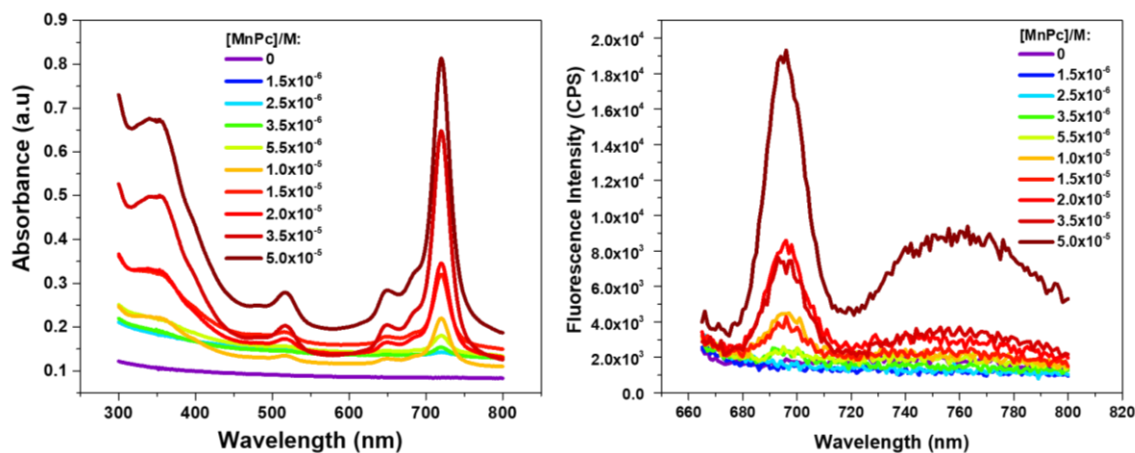


Figure 20. Spectral changes upon the addition of variable concentration of MnPc (0 to  $5 \times 10^{-5}$  M) to 0.05 mg/mL of MWCNT in CBZ. Left: Absorption Spectrum; Right: Emission Spectrum,  $\lambda_{ex} = 650$  nm.

### 3.3.3. MWCNT-PCPDTBT titration

The titration experiment of MWCNT with the donor PCPDTBT can be evidenced in Figure 21. Again, with increasing concentration of PCPDTBT the absorbance increases. However, like MnPc close to the end of titration there is an observation of spectral crossover (light red traces in Figure 21 left, showing crossover around 600 nm). Also, the fluorescence spectra, Figure 21

right shows quenching at the concentrations where the absorption spectra showed crossover indicative of an associative interaction between the donor and acceptor. We are being careful in using the term ‘isosbestic point’ and rather ‘crossover’ as we presume that the complex formation might have simply happened at a certain concentration rather than a smooth transition.

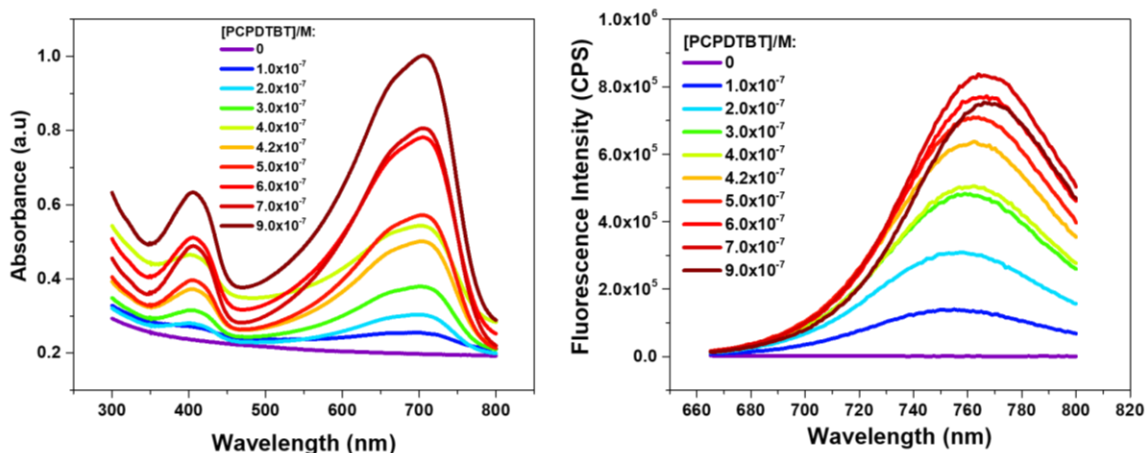


Figure 21. Spectral changes upon the addition of variable concentration of PCPDTBT ( $0$  to  $9 \times 10^{-7}$  M) to  $0.05$  mg/mL of MWCNT in CBZ. Left: Absorption Spectrum; Right: Emission Spectrum,  $\lambda_{ex} = 650$  nm.

### 3.3.4. Acceptor-Donor Binding Constants, $K$ .

The binding constants ( $K$ ) were calculated using the Benesi-Hilderbrand (BH) equation (equation 1, chapter 2.1) obtained both from absorption and fluorescence data by fitting them to a 1:1 complex. Table 4 shows the binding constants for the complex formation and the plots in Figure 22 were used for the determination of  $K$ .

From the fluorescence binding constant values of  $H_2Pc$  it can be concluded that MWCNT has high affinity for association in the current study than that from the literature, where  $H_2Pc-PyC_{60}$  complex gave a binding constant of  $5.60 \times 10^3 \text{ M}^{-1}$  [105]. Similarly,  $MnPc$  binds effectively to MWCNT herein when compared to naphthoquinone derivative (I) with I- $MnPc$  binding constant of  $2.06 \times 10^3 \text{ M}^{-1}$  [106]. Furthermore, the MWCNT-PCPDTBT blend indicates exceptionally high binding constant values corroborating the formation of supramolecular complex which is in conjunction with the observed behaviour during the absorption and emission titrations.

Table 4. The UV-vis and fluorescence binding constant of complexes that formed at 650nm (absorption and emission) recorded in chlorobenzene.

Blends	$K_{UV-vis} (M^{-1})$	$K_{Fluorescence} (M^{-1})$
MWCNT-H <sub>2</sub> Pc	$0.864 \times 10^3$	$1.14 \times 10^6$
MWCNT-MnPc	$5.42 \times 10^3$	$3.50 \times 10^4$
MWCNT-PCPDTBT	$4.33 \times 10^5$	$1.03 \times 10^6$

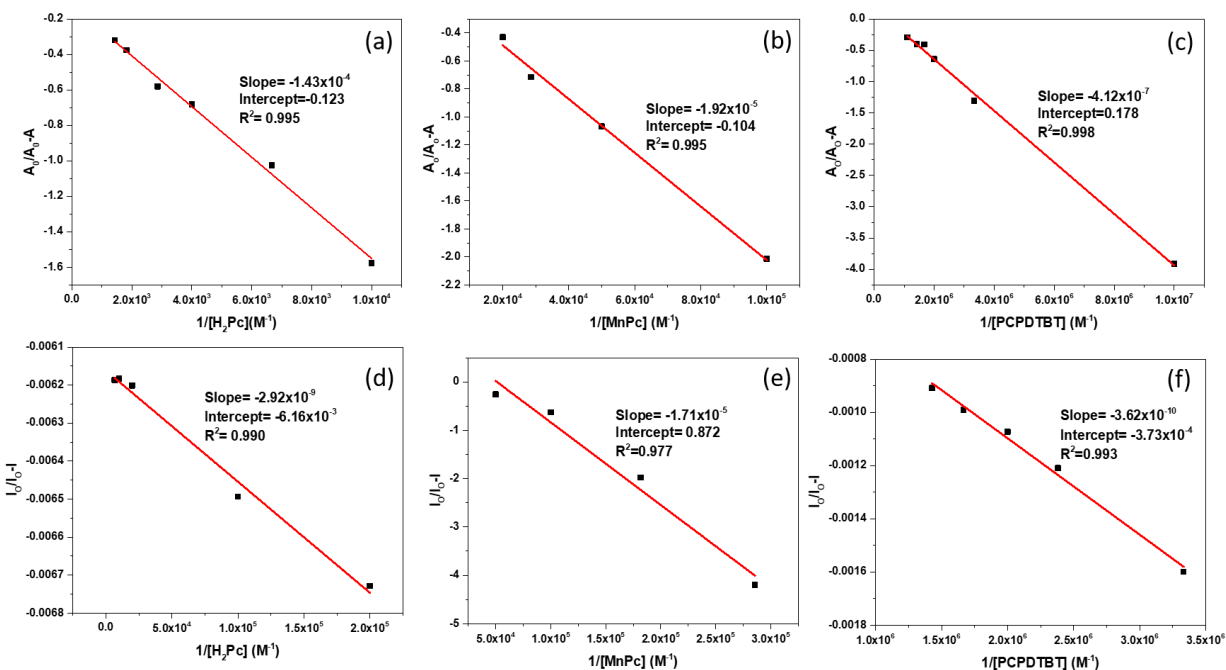


Figure 22. A plot of  $A_0/A_0-A$  vs. inverse conversation of the donor – (a) H<sub>2</sub>Pc, (b) MnPc, (c) PCPDTBT and  $I_0/I_0-I$  vs. inverse concentration of the donor – (d) H<sub>2</sub>Pc, (e) MnPc, (f) PCPDTBT, at a constant MWCNT concentration (0.05 mg/mL) collected in CBZ solvent.

### 3.4. Electrochemical measurements

#### 3.4.1. Cyclic voltammetry (CV) and Differential Pulse Voltammogram (DPV) of pristine donors (H<sub>2</sub>Pc, MnPc and PCPDTBT)

The redox properties of pristine donor compounds; namely, H<sub>2</sub>Pc, MnPc and PCPDTBT, were studied using both cyclic- and differential pulse voltammetry. Voltammetric measurements are beneficial for the analysis of electrochemical properties of materials since it allows for an

investigation of potentials in both oxidative and reductive directions. The voltammetric measurements were recorded in *ortho*-dichlorobenzene (*o*-DCB) with 0.01 M tetrabutylammonium hexafluorophosphate (TBAPF<sub>6</sub>) as a supporting working electrolyte, glassy carbon electrode as working electrode and Fc/Fc<sup>+</sup> as internal standard. All the Figures shown in the present study DPVs, and CVs were initially run to set the window for DPV. Further the concentrations reported here are those at which the voltammograms were well resolved with readable current values.

The voltammetric features of M-Pcs generally arises due to the CT in the macrocyclic ring, and between the metal and ring whereas in metal-free phthalocyanine (H<sub>2</sub>Pc) they arise as a result of CT macrocyclic ring only [66].

The DPV of H<sub>2</sub>Pc in figure 23 reveals two sequential oxidative events at 0.94 and 1.43 V vs. Fc/Fc<sup>+</sup> and two sequential reduction events at -1.15 and -1.45 V vs. Fc/Fc<sup>+</sup>. This compares very well with those obtained in literature reported to be 0.94 and 1.34 V vs. SCE and -0.74 and -0.99 V vs SCE for a ternary ammonium substituted phthalocyanine system [107]. In addition, the H<sub>2</sub>Pc oxidative and reductive waves are reversible which was supported by our cyclic voltammetric measurements where,  $\Delta E = E_{pa} - E_{pc}$  obtained to be 78 mV, 118 mV respectively. These are typical Pc ring/substituent oxidations and Pc ring reduction of H<sub>2</sub>Pc.

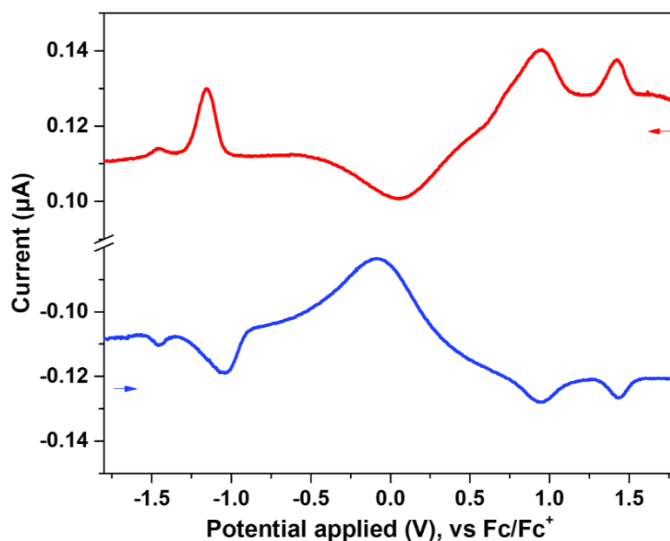


Figure 23. DPV of H<sub>2</sub>Pc; Conc.  $1.16 \times 10^{-4}$  M; DPV parameters: pulse height: 10 mV, scan rate 0.01 V/s.

The voltammetric behaviour of MnPc is shown in Figure 24. Two oxidative events are observed at 0.42 and 0.94 V whereas in literature the peaks appear shifted at 0.85 and 1.1 V vs. SCE [108]. On the other hand, three reductive events are seen at -0.45, -1.29 and -1.72 V vs Fc/Fc<sup>+</sup>. The first reductive event can be attributed to the electron transfer from Pc ring to Mn (metal reduction event) [109] while the rest of the two Pc ring reduction events are shifted to more negative potentials compared to that of H<sub>2</sub>Pc due to the metal substitution in the MnPc. It is established in literature that unsubstituted MnPc is very unstable [98] and one has to work within a time scale of 4 h to get a reasonable data. Hence, MnPc is generally extensively substituted and based on the substituent groups, heavy changes to the redox behaviour can be seen.

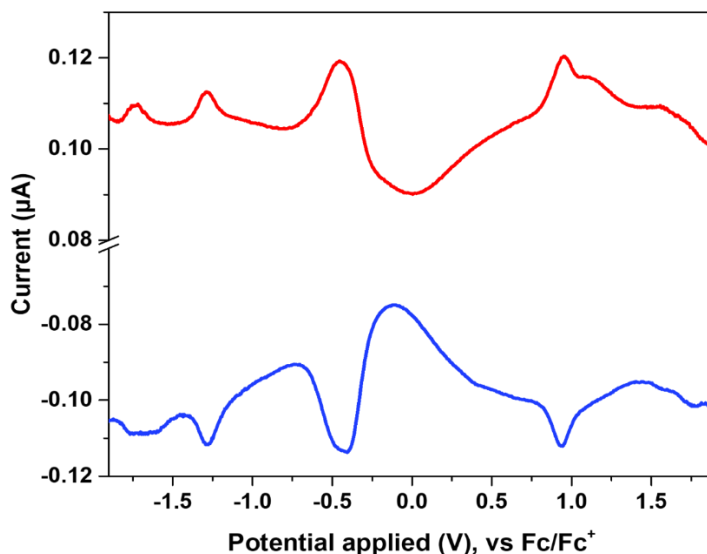


Figure 24. DPV of MnPc; Conc.  $9.83 \times 10^{-5}$  M; DPV parameters: pulse height: 10 mV, scan rate 0.01 V/s.

Based on the results in CV experiments, we ran the DPVs for PCPDTBT and the voltammograms revealed that the system is reversible with the difference between the anodic and cathodic peak,  $\Delta E = E_{pa} - E_{pc}$ , to be 55 mV. Figure 25 reveals the voltammograms where anodic features are seen 0.5 V and the cathodic features at -1.37 and -1.57 V. This is in agreement with literature where the experiments were done at similar conditions [101]. It is worth mentioning here that the oxidative potential is in a well accessible low energy region confirming that PCBDTBT is a good donor which is why it found an application in OPVs with fullerenes as acceptors.

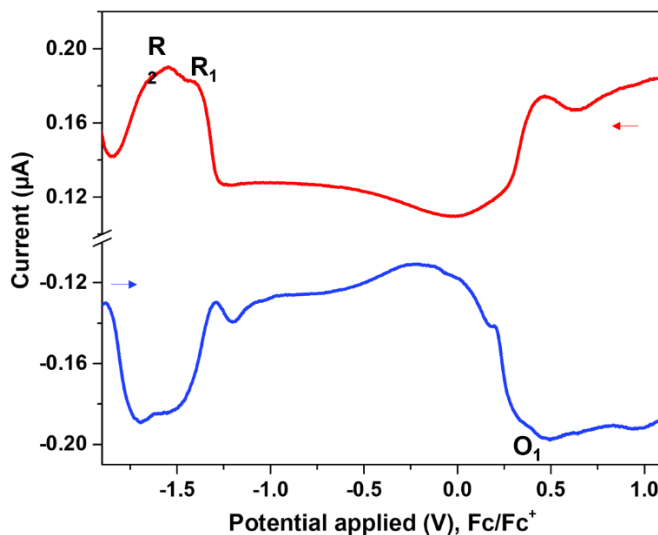


Figure 25. DPV of PCPDTBT; Conc.  $1.23 \times 10^{-6}$  M; DPV parameters: pulse height: 10 mV, scan rate 0.01 V/s.

While analysing the band gaps of these donor materials, we confirmed from literature that the addition of the central metal on the macrocyclic ring of Pc aids a decrease in the energy band gap (Table 5). While Table 5 shows that PCPDTBT band gaps compare well with the one provided in literature, given by 1.73 V vs. NHE [101], the presence of thiophene rings explains the reduction of the gap contrast to the one observed for a similar type of polymer, P3OT ( $E_{\text{gap}} = 1.83$  eV) [27, 110].

Table 5. Optical band gap ( $E_{\text{gap}}^{\text{Opt}}$ ) and electrical band gap ( $E_{\text{gap}}^{\text{Echem}}$ ) of pristine donor compounds.

Donors	$E_{\text{gap}}^{\text{Opt}*}$ (eV)	$E_{\text{gap}}^{\text{Echem}*}$ (eV)
H <sub>2</sub> Pc	1.74	2.01
MnPc	1.65	1.78
PCPDTBT	1.59	2.05

\*Energy gaps were calculated using  $E_{\text{HOMO/LUMO}} = e(E_{\text{Ox/Red}} - E_{1/2}(\text{Fc/Fc}^+)) + 4.8$  eV [110]



### 3.4.2. DPV Measurements for A-D complexes

The electrochemical behaviour while complexes were being formed was analysed by performing an electrochemical titration using DPV by a sequential addition of MWCNT to a fixed concentration of the respective donors. Herein, as opposed to spectrometric titrations, the acceptor was kept constant because MWCNT did not reveal any redox behaviour and the movement of the voltammetric features of the donor is expected to indicate an interaction between the A and D. , The voltammetric titration of donors ( $H_2Pc$ ,  $MnPc$  and  $PCPDTBT$ ) with MWCNT (0 – 4 mL aliquots of 0.05 mg/mL) was recorded in o-DCB with 0.01 M TBA- $PF_6$  as a supporting working electrolyte.

The voltammetric changes of  $H_2Pc$  upon addition of MWCNT show a noteworthy shift of the first oxidative step in anodic direction (Figure 26), with the change in potential shift ( $\Delta E$ ) observed to be 107 mV (Table 6). This shift can be attributed to the rise in the  $H_2Pc$  energy of LUMO level [111] because of the transfer of charge to the acceptor thus forming MWCNT-  $H_2Pc$  supramolecular complex. The increase in LUMO energy level is from 3.43 to 3.55 eV which is the resultant of electron donation from the donor to the acceptor.

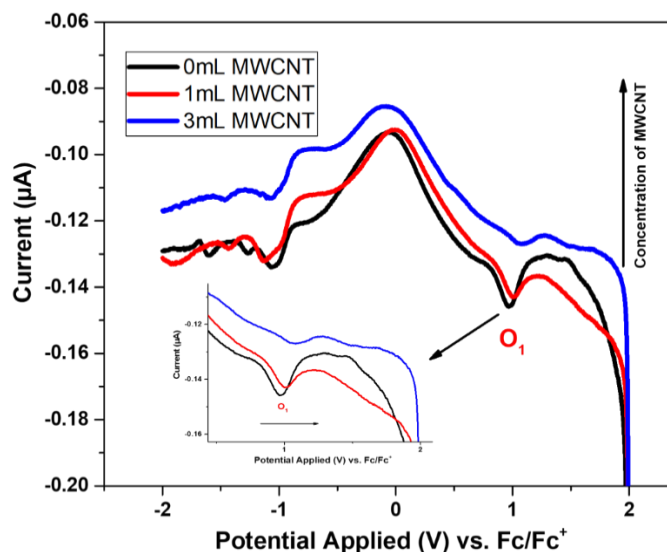


Figure 26. Differential pulse voltammogram of  $H_2Pc$  ( $1 \times 10^{-4}$  M) with variable concentration of MWCNT (0 – 3 mL aliquots of 0.05 mg/mL) at 10 mV pulse amplitude, 10 mV/s scan rate on a glassy carbon electrode in oDCB: TBA- $PF_6$  solution; The inset shows the zoomed in DPV of  $H_2Pc$  indicating the movement of anodic peak.

Table 6. Electrochemical titration of donors with increasing concentration of MWCNT (0 – 3 mL aliquots of 0.05 mg/mL) in oDCB: TBA-PF<sub>6</sub> solution results.

MWCNT Additions (mL)	H <sub>2</sub> Pc	MnPc	PCPDTBT
	E <sub>ox,1</sub> (V)	E <sub>ox,1</sub> (V)	E <sub>ox,1</sub> (V)
0	0.971	1.019	0.459
1	1.008	1.026	0.469
3	1.078	1.057	0.477*

\*Is the E<sub>ox</sub> of PCPDTBT after the 4<sup>th</sup> MWCNT addition.

The electrochemical titration of MnPc with MWCNT follows a similar trend as shown for MWCNT-H<sub>2</sub>Pc voltammetric changes, especially with the second oxidative. As evidenced in Figure 27, the first oxidative peak disappears with the addition of MWCNT. Thus, the overall electrochemical features support the charge transfer and the formation of MWCNT-MnPc supramolecular complexes, with the 2<sup>nd</sup> oxidative peak potential shift ( $\Delta E$ ) obtained to be 38 mV (Table 6). The presence of CT is also supported by the increase in the LUMO energy level, going from 3.30 to 3.43 eV.

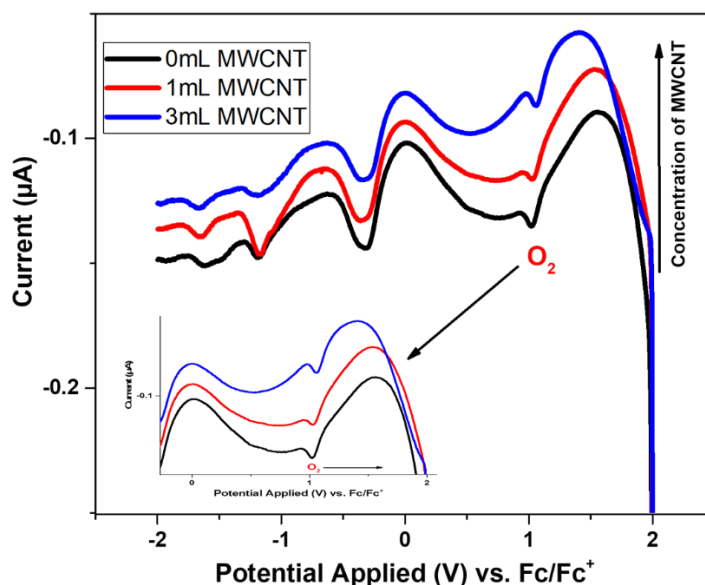


Figure 27. Differential pulse voltammogram of MnPc ( $1 \times 10^{-4}$  M) with variable concentration of MWCNT (0 – 3 mL aliquots of 0.05 mg/mL) at 10 mV pulse amplitude, 10 mV/s scan rate on a glassy carbon electrode in o-DCB: TBA-PF<sub>6</sub> solution; The inset shows the zoomed in DPV of MnPc indicating the movement of anodic peak.

The voltammetric changes upon addition of MWCNT to PCPDTBT solutions is shown in Figure 28. Again, the oxidative peak potential shift in the anodic direction. On average the O<sub>1</sub> peak shifts from 0.459 V to 0.477 V with the potential shift ( $\Delta E$ ) being 18 mV. In overall it can be concluded that there is CT between PCPDTBT and MWCNT, thus the formation of PCPDTBT supramolecular complexes. Lastly, it is notable that the voltammograms shows a decrease in the oxidative peak current upon the addition of variable concentrations of MWCNT, Figures 26, 27, 28). This can be attributed to the formation of complexes with smaller diffusion coefficients [112, 113].

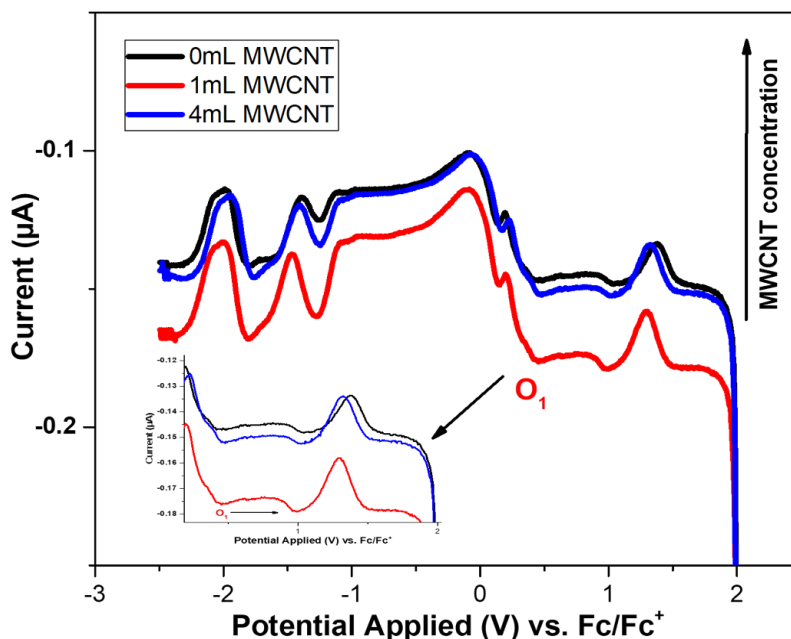


Figure 28. Differential pulse voltammogram of PCPDTBT ( $1 \times 10^{-4}$  M) with variable concentration of MWCNT (0 – 4 mL aliquots of 0.05 mg/mL) at 10 mV pulse amplitude, 10 mV/s scan rate on a glassy carbon electrode in o-DCB: TBA-PF<sub>6</sub> solution; The inset shows the zoomed in DPV of PCPDTBT indicating the movement of anodic peak.

### 3.4.3. Electrochemical Acceptor-Donor Binding Constants, $K$ .

The binding constants were calculated using the equation [112],

$$\frac{1}{C_{MWCNT}} = \frac{K(1-A)}{1-\frac{i}{i_0}} - K,$$

with  $C_{MWCNT}$  the variable concentration of MWCNT,  $K$  is the binding constant,  $i$  and  $i_0$  the peak current with and without MWCNT respectively, while  $A$  is the proportionality constant.

The electrochemical binding constants as seen in Table 7 show evidence of CT thus formation of the supramolecular complexes. It is seen that the binding constants of MWCNT-H<sub>2</sub>Pc complex is much smaller than that of the MWCNT-MnPc complex. The central metal in the macrocyclic ring contributes to the electron density and thus the charge transfer [66], and hence high binding constant. Although the blends of MWCNT- (MnPc/ PCPDTBT) binding constants are high, these values are much smaller than the ones obtained from spectrophotometric method (Table 4). Nevertheless, it is worth noting that the PCPDTBT and MnPc does show good promise as donors keeping to the trend in binding constant values.

Table 7. The binding constant (*K*) from electrochemical titration of donors with increasing concentration of MWCNT in *o*DCB: TBA-PF<sub>6</sub> solution.

Blends	<i>K</i>
MWCNT-H <sub>2</sub> Pc	14.23
MWCNT-MnPc	126.20
MWCNT-PCPDTBT	101.24

### 3.5. Transmission electron microscopy measurements

Transmission electron microscopic method was used to visualize the structural changes/formation when such supramolecular systems are prepared exploiting their non-covalent interactions. The TEM images were obtained for the concentrations of the titration mix where we saw crossover in absorption spectroscopic peaks. A carbon coated copper grid was used as a substrate where a single drop of the mixture was placed and allowed to air dry before being exposed to the imaging. It has been shown in literature [114] that the MWCNT show long wire like formation while the phthalocyanines show whisker/rod like structures [115]. While these two interact with each other, we expect a decoration of MWCNT surface with MPcs (M = H<sub>2</sub> or Mn). This was indeed the case in our studies as well. Figure 29(a) shows the phthalocyanines distributed as rods and one of the darker areas in the image was zoomed and contrasted to give Figure 29 (b) which shows the nanotubes as reported in literature [116].

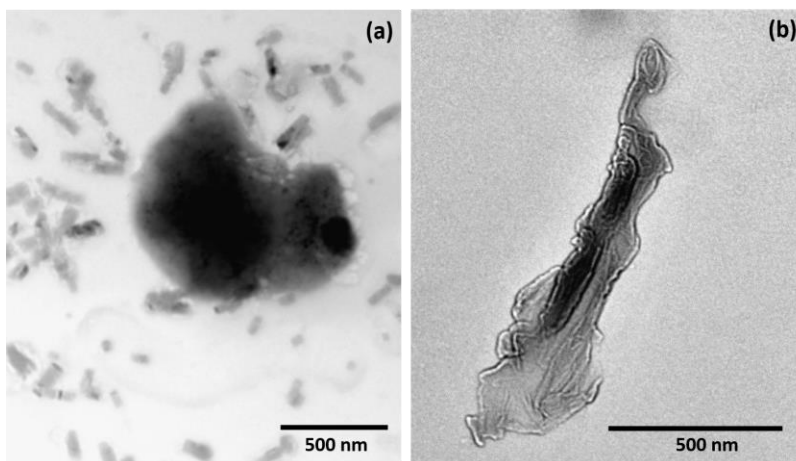


Figure 29. TEM image of  $H_2Pc$  – MWCNT complex taken at the concentration where crossover was observed in absorption measurements. Please refer to the explanation in the main text for (a) and (b).

The TEM image of MnPc-MWCNT complex can be seen from Figure 30 which also gives a similar observation. Since the TEM instrument is of low resolution the images obtained were not more than 200 nm resolution, however they did indicate the association between the compounds studied.

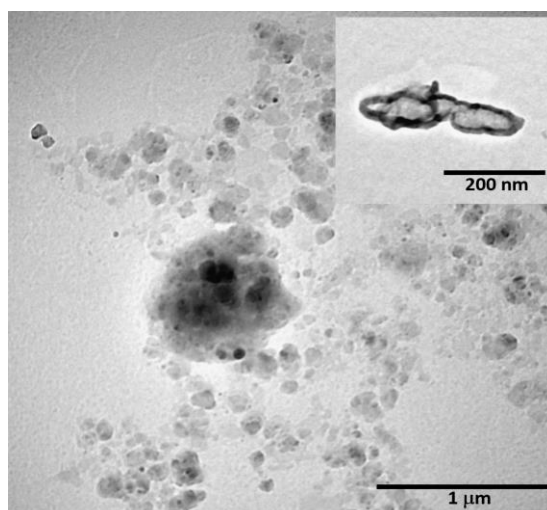
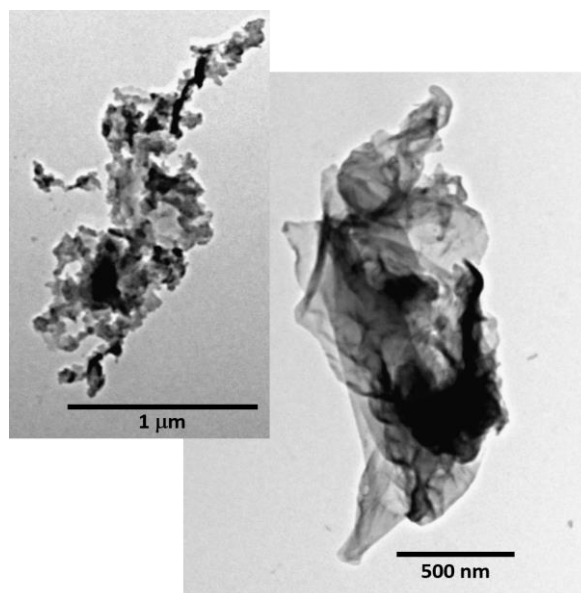


Figure 30. TEM image of MnPc – MWCNT complex taken at the concentration where crossover was observed in absorption measurements. The inset shows the zoomed portion of one of the selected darker areas which reveal the presence of MWCNT.

It is further known in literature the PCPDTBT is capable of forming branched structures as it is a polymer [117]. However, in our study we could not see that due to the low resolution of the instrument (Figure 31). Nevertheless, we could discern the MWCNT intertwined with helical

patterns of PCPBTBT which indicated their association. Thus, we conclude that we do see associative interaction between the acceptor MWCNT and the donors.



*Figure 31. TEM image of PCPDTBT – MWCNT complex taken at the concentration where crossover was observed in absorption measurements. The right image shows the zoomed portion of one of the selected darker areas which reveal the presence of MWCNT intertwined with PCPDTBT.*

## Chapter 4

### 4. Conclusion and Future work

#### 4.1. Conclusion

The physicochemical interactions between MWCNT and donors (H<sub>2</sub>Pc, MnPc and PCPDTBT) were investigated and it was found that there is interaction thus formation of MWCNT-Donor supramolecular complexes using absorption, fluorescence and voltammetric techniques. Despite MnPc unstable nature, the spectrophotometric and voltammetric binding constant values show favourable association with MWCNT. The molar extinction coefficient, quantum yield and binding constant depicts the material's potential. Particularly, its high absorption at lower energies and small bandgap seen in this study are central to the fabrication of OPV devices. Furthermore, manganese is the 5<sup>th</sup> most abundant metal therefore these factors should invoke further investigation. The effect of small bandgap on polymeric donors allowing them to absorb significant section of the solar spectrum is confirmed by PCPDTBT's remarkable molar extinction coefficient and quantum yield, similarly the impact of the polymer's conjugated backbone increases its affinity to donate electrons to electron deficient materials, in this case MWCNT. This is confirmed from high binding constants reported in this study.

#### 4.2. Future work

Donor-acceptor supramolecular complexes can be investigated further using fluorescence lifetime, Femtosecond transient absorption spectroscopy and theoretical calculations to help gain in-depth understanding of electron transfer processes and their lifetimes and thus the photoinduced complexes that form. In addition, investigate the stability of substituted MnPc compared to its unsubstituted counterpart. Also, a high-resolution TEM imaging with selected area diffraction studies will be able to shine light onto the nature of association and crystallinity of the complexes involved. This will greatly help in understanding the photocurrent produced when a device is made from these systems, as the nature of the structures formed decide the flow of currents.

## References

1. Firoozabadi, A. and P.C. Myint, *Prospects for subsurface CO<sub>2</sub> sequestration*. AIChE journal, 2010. **56**(6): p. 1398-1405.
2. Doney, S.C., et al., *Ocean acidification: the other CO<sub>2</sub> problem*. 2009.
3. Boyd, R., N. Stern, and B. Ward, *What will global annual emissions of greenhouse gases be in 2030, and will they be consistent with avoiding global warming of more than 2 C?* 2015.
4. Lashof, D.A. and D.R. Ahuja, *Relative contributions of greenhouse gas emissions to global warming*. Nature, 1990. **344**(6266): p. 529-531.
5. Hlongwane, M.H., *Single and double layer bulk heterojunction organic solar cell*. 2015.
6. Pather, V. *Eskom and water*. in *Proceedings of the 2004 Water Institute of Southern Africa (WISA) Biennial Conference, Cape Town, South Africa*. URL: <http://www.ewisa.co.za/literature/files/260.pdf> (Accessed 1 October 2020). 2004.
7. Makgetla, N. and M. Patel, *The coal value chain in South Africa*. Trade & industrial Policy Strategies. Pretoria, 2021.
8. Otieno, F.A. and G.M. Ochieng, *Water management tools as a means of averting a possible water scarcity in South Africa by the year 2025*. Water Sa, 2004. **30**(5): p. 120-124.
9. Jamal, N., *Options for the supply of electricity to rural homes in South Africa*. Journal of Energy in Southern Africa, 2015. **26**(3): p. 58-65.
10. Lissette, F., *Highlights of a visit to South Africa's 'Adventure Province' – Eastern Cape Province*. N/A, Frank & Lissette.
11. Chapin, D.M., C. Fuller, and G. Pearson, *A new silicon p-n junction photocell for converting solar radiation into electrical power*. Journal of Applied Physics, 1954. **25**(5): p. 676-677.
12. Green, M.A., et al., *Solar cell efficiency tables (version 51)*. Progress in photovoltaics: research and applications, 2018. **26**(1): p. 3-12.
13. de la Torre, G., G. Bottari, and T. Torres, *Phthalocyanines and subphthalocyanines: Perfect partners for fullerenes and carbon nanotubes in molecular photovoltaics*. Advanced Energy Materials, 2017. **7**(10): p. 1601700.
14. Kumar, P. and S. Chand, *Recent progress and future aspects of organic solar cells*. Progress in Photovoltaics: Research and applications, 2012. **20**(4): p. 377-415.
15. Blom, P.W., et al., *Device physics of polymer: fullerene bulk heterojunction solar cells*. Advanced Materials, 2007. **19**(12): p. 1551-1566.
16. Tang, C.W., *Two-layer organic photovoltaic cell*. Applied Physics Letters, 1986. **48**(2): p. 183-185.
17. Kumar, M. and S. Kumar, *Liquid crystals in photovoltaics: a new generation of organic photovoltaics*. Polymer Journal, 2017. **49**(1): p. 85-111.
18. Sariciftci, N.S., et al., *Photoinduced electron transfer from a conducting polymer to buckminsterfullerene*. Science, 1992. **258**(5087): p. 1474-1476.
19. Sharma, G., P. BalaRaju, and M. Roy, *Effect of functional groups of acceptor material on photovoltaic response of bulk hetero-junction organic devices based on tin phthalocyanine (SnPc)*. Solar energy materials and solar cells, 2008. **92**(3): p. 261-272.
20. Yu, G., et al., *Polymer photovoltaic cells: enhanced efficiencies via a network of internal donor-acceptor heterojunctions*. Science, 1995. **270**(5243): p. 1789-1791.
21. Schultes, S., et al., *The role of molecular architecture and layer composition on the properties and performance of CuPc-C60 photovoltaic devices*. Materials Science and Engineering: C, 2005. **25**(5-8): p. 858-865.
22. Zhang, Y., et al., *The electronic structures and optical properties of fullerene derivatives for organic solar cells: The number and size effects of fullerene-cage*. Materials Chemistry and Physics, 2018. **204**: p. 95-104.
23. Andrew J. Ferguson, J.L.B., Nikos Kopidakis, *Fullerenes and carbon nanotubes as acceptor materials*



in organic photovoltaics. Elsevier B.V, 2012. **90**: p. 115-125

24. Brabec, C.J., *Organic photovoltaics: technology and market*. Solar energy materials and solar cells, 2004. **83**(2-3): p. 273-292.
25. Dang, M.T., L. Hirsch, and G. Wantz, *P3HT: PCBM, best seller in polymer photovoltaic research*. Advanced Materials, 2011. **23**(31): p. 3597-3602.
26. Kadem, B., W. Cranton, and A. Hassan, *Metal salt modified PEDOT: PSS as anode buffer layer and its effect on power conversion efficiency of organic solar cells*. Organic Electronics, 2015. **24**: p. 73-79.
27. Kroon, R., et al., *Small bandgap polymers for organic solar cells (polymer material development in the last 5 years)*. Polymer Reviews, 2008. **48**(3): p. 531-582.
28. Ala'a, F.E., et al., *Recent advances of non-fullerene, small molecular acceptors for solution processed bulk heterojunction solar cells*. Journal of Materials Chemistry A, 2014. **2**(5): p. 1201-1213.
29. Jarzab, D., et al., *Low-Temperature Behaviour of Charge Transfer Excitons in Narrow-Bandgap Polymer-Based Bulk Heterojunctions*. Advanced Energy Materials, 2011. **1**(4): p. 604-609.
30. Soci, C., et al. *Charge carrier photogeneration and transport properties of a novel low-bandgap conjugated polymer for organic photovoltaics*. in *Organic Photovoltaics VII*. 2006. International Society for Optics and Photonics.
31. Holliday, S., et al., *High-efficiency and air-stable P3HT-based polymer solar cells with a new non-fullerene acceptor*. Nature communications, 2016. **7**: p. 11585.
32. Soci, C., et al., *Photoconductivity of a low-bandgap conjugated polymer*. Advanced Functional Materials, 2007. **17**(4): p. 632-636.
33. Sun, Y., et al., *Solution-processed small-molecule solar cells with 6.7% efficiency*. Nature materials, 2012. **11**(1): p. 44-48.
34. Kietzke, T., et al., *Effect of annealing on the characteristics of organic solar cells: polymer blends with a 2-vinyl-4, 5-dicyanoimidazole derivative*. Macromolecules, 2007. **40**(13): p. 4424-4428.
35. Holliday, S., et al., *A rhodanine flanked nonfullerene acceptor for solution-processed organic photovoltaics*. Journal of the American Chemical Society, 2015. **137**(2): p. 898-904.
36. Arabnejad, S., et al., *Effect of nuclear motion on charge transport in fullerenes: a combined density functional tight binding—density functional theory investigation*. Frontiers in Energy Research, 2019. **7**: p. 3.
37. Wang, Y., et al., *Ternary blend solar cells based on a conjugated polymer with diketopyrrolopyrrole and carbazole units*. Frontiers in Energy Research, 2018. **6**: p. 113.
38. Muhammad, F.F., *Design approaches to improve organic solar cells*. Journal of Technology Innovations in Renewable Energy, 2014. **3**(2): p. 63-71.
39. Shiraishi, M. and M. Ata, *Work function of carbon nanotubes*. Carbon, 2001. **39**(12): p. 1913-1917.
40. El-Sayed, B.A., et al., *Photocatalytic study of some synthesized MWCNTs/TiO<sub>2</sub> nanocomposites used in the treatment of industrial hazard materials*. Egyptian Journal of Petroleum, 2019. **28**(2): p. 247-252.
41. Lee, S.J., et al., *Effects of MEH-PPV Molecular Ordering in the Emitting Layer on the Luminescence Efficiency of Organic Light-Emitting Diodes*. Molecules, 2021. **26**(9): p. 2512.
42. Guan, Z.-L., et al., *Direct determination of the electronic structure of the poly (3-hexylthiophene): phenyl-[6, 6]-C61 butyric acid methyl ester blend*. Organic Electronics, 2010. **11**(11): p. 1779-1785.
43. Li, R., et al., *Electron-donating or-withdrawing nature of substituents revealed by the electrochemistry of metal-free phthalocyanines*. Inorganic chemistry, 2006. **45**(5): p. 2327-2334.

44. Hussein, M., *Theoretical IR spectroscopic study of Copper Phthalocyanine (CuPc)*. Al-Nahrain Journal for Engineering Sciences, 2008. **11**(2): p. 303-306.
45. Prushan, M., *Absorption and Fluorescence Spectroscopy of Tetraphenylporphyrin and Metallo-Tetraphenylporphyrin, 2005*.
46. Basiuk, E.V., L. Huerta, and V.A. Basiuk, *Noncovalent bonding of 3d metal (II) phthalocyanines with single-walled carbon nanotubes: a combined DFT and XPS study*. Applied Surface Science, 2019. **470**: p. 622-630.
47. Sahoo, S.R., S. Sahu, and S. Sharma, *Charge transport and prototypical optical absorptions in functionalized zinc phthalocyanine compounds: A density functional study*. Journal of Physical Organic Chemistry, 2018. **31**(4): p. e3785.
48. Granström, M., et al., *Laminated fabrication of polymeric photovoltaic diodes*. Nature, 1998. **395**(6699): p. 257-260.
49. Menke, S.M. and R.J. Holmes, *Exciton diffusion in organic photovoltaic cells*. Energy & Environmental Science, 2014. **7**(2): p. 499-512.
50. Tamai, Y., et al., *Exciton diffusion in conjugated polymers: from fundamental understanding to improvement in photovoltaic conversion efficiency*. The journal of physical chemistry letters, 2015. **6**(17): p. 3417-3428.
51. Markov, D.E., et al., *Accurate measurement of the exciton diffusion length in a conjugated polymer using a heterostructure with a side-chain cross-linked fullerene layer*. The Journal of Physical Chemistry A, 2005. **109**(24): p. 5266-5274.
52. Savenije, T.J., J.M. Warman, and A. Goossens, *Visible light sensitisation of titanium dioxide using a phenylene vinylene polymer*. Chemical physics letters, 1998. **287**(1-2): p. 148-153.
53. Terao, Y., H. Sasabe, and C. Adachi, *Correlation of hole mobility, exciton diffusion length, and solar cell characteristics in phthalocyanine/fullerene organic solar cells*. Applied Physics Letters, 2007. **90**(10): p. 103515.
54. Braun, C.L., *Electric field assisted dissociation of charge transfer states as a mechanism of photocarrier production*. The Journal of chemical physics, 1984. **80**(9): p. 4157-4161.
55. Brabec, C.J., et al., *Origin of the open circuit voltage of plastic solar cells*. Advanced Functional Materials, 2001. **11**(5): p. 374-380.
56. Rand, B.P., D.P. Burk, and S.R. Forrest, *Offset energies at organic semiconductor heterojunctions and their influence on the open-circuit voltage of thin-film solar cells*. Physical Review B, 2007. **75**(11): p. 115327.
57. Peumans, P. and S.R. Forrest, *Separation of geminate charge-pairs at donor-acceptor interfaces in disordered solids*. Chemical Physics Letters, 2004. **398**(1-3): p. 27-31.
58. Saifuddin, N., A. Raziah, and A. Junizah, *Carbon nanotubes: a review on structure and their interaction with proteins*. Journal of Chemistry, 2013. **2013**.
59. Njuguna, J., O.A. Vanli, and R. Liang, *A review of spectral methods for dispersion characterization of carbon nanotubes in aqueous suspensions*. Journal of Spectroscopy, 2015. **2015**.
60. Skakalova, V., U. Dettlaff-Weglikowska, and S. Roth, *Electrical and mechanical properties of nanocomposites of single wall carbon nanotubes with PMMA*. Synthetic metals, 2005. **152**(1-3): p. 349-352.
61. Girek, B. and W. Sliwa, *Hybrids of cationic porphyrins with nanocarbons*. Journal of inclusion phenomena and macrocyclic chemistry, 2015. **82**(3-4): p. 283-300.
62. Bhatia, R. and L. Kumar, *Functionalized carbon nanotube doping of P3HT: PCBM photovoltaic devices for enhancing short circuit current and efficiency*. Journal of Saudi Chemical Society, 2017. **21**(3): p. 366-376.
63. Xiao, Y., et al., *Pulse electropolymerization of high performance PEDOT/MWCNT counter electrodes for Pt-free dye-sensitized solar cells*. Journal of Materials Chemistry, 2012. **22**(37): p. 19919-19925.

64. Agrawal, S. and M.K.G. Rai, *Performance analysis of multi walled carbon nanotube (MWCNT) bundle as VLSI interconnects*. 2015.
65. Shariati, M.-N., *Electronic and geometric structure of phthalocyanines on Metals*. 2012, Acta Universitatis Upsaliensis.
66. Orman, E.B., et al., *Electrochemical, electrocatalytic dioxygen reducing and dielectric relaxation properties of non-peripheral tetra-2, 3-dihydro-1H-inden-5-yloxy substituted phthalocyanines*. Journal of The Electrochemical Society, 2015. **162**(12): p. H825.
67. Travis, A.S., E. Center, and L. Baeck, *Mauve and its anniversaries*. Bulletin for the History of Chemistry, 2007. **32**(1): p. 35-44.
68. Dahlen, M.A., *The phthalocyanines a new class of synthetic pigments and dyes*. Industrial & Engineering Chemistry, 1939. **31**(7): p. 839-847.
69. Bıyıklıoğlu, Z., et al., *Synthesis, characterization and electrochemistry of a new organosoluble metal-free and metallophthalocyanines*. Polyhedron, 2008. **27**(6): p. 1707-1713.
70. Alfredsson, Y., et al., *Electronic structure of a vapor-deposited metal-free phthalocyanine thin film*. The Journal of chemical physics, 2005. **122**(21): p. 214723.
71. Lin, C.-L., C.-C. Lee, and K.-C. Ho, *Spectroelectrochemical studies of manganese phthalocyanine thin films for applications in electrochromic devices*. Journal of electroanalytical Chemistry, 2002. **524**: p. 81-89.
72. Murata, K., et al., *Long-lived excited state of C60 in C60/phthalocyanine heterojunction solar cell*. Applied physics letters, 1996. **68**(3): p. 427-429.
73. Liao, M.-S. and S. Scheiner, *Electronic structure and bonding in metal phthalocyanines, metal= Fe, Co, Ni, Cu, Zn, Mg*. The Journal of Chemical Physics, 2001. **114**(22): p. 9780-9791.
74. Harun, M.H., et al., *Conjugated conducting polymers: A brief overview*. UCSI Academic Journal: Journal for the Advancement of Science & Arts, 2007. **2**: p. 63-68.
75. Heeger, A.J., *Semiconducting polymers: the third generation*. Chemical Society Reviews, 2010. **39**(7): p. 2354-2371.
76. Petsagkourakis, I., et al., *Structurally-driven enhancement of thermoelectric properties within poly (3, 4-ethylenedioxythiophene) thin films*. Scientific reports, 2016. **6**: p. 30501.
77. Sethumadhavan, V., et al., *Hydrolysis of doped conducting polymers*. Communications Chemistry, 2020. **3**(1): p. 1-9.
78. Shrotriya, V., et al., *Accurate measurement and characterization of organic solar cells*. Advanced functional materials, 2006. **16**(15): p. 2016-2023.
79. Li, G., et al., *High-efficiency solution processable polymer photovoltaic cells by self-organization of polymer blends*, in *Materials For Sustainable Energy: A Collection of Peer-Reviewed Research and Review Articles from Nature Publishing Group*. 2011, World Scientific. p. 80-84.
80. Colladet, K., et al., *Low band gap donor– acceptor conjugated polymers toward organic solar cells applications*. Macromolecules, 2007. **40**(1): p. 65-72.
81. Peet, J., et al., *Efficiency enhancement in low-bandgap polymer solar cells by processing with alkane dithiols*. Nature materials, 2007. **6**(7): p. 497-500.
82. Albrecht, S., et al., *Light management in PCPDTBT: PC70BM solar cells: A comparison of standard and inverted device structures*. Organic Electronics, 2012. **13**(4): p. 615-622.
83. Company, C.-P.R.A.S. *Spectroscopy Applications Selection Guide*. 2020 [cited 2021 21/11]; Available from: <https://www.coleparmer.com/tech-article/spectroscopy-selection-guide>.
84. Benesi, H.A. and J. Hildebrand, *A spectrophotometric investigation of the interaction of iodine with aromatic hydrocarbons*. Journal of the American Chemical Society, 1949. **71**(8): p. 2703-2707.
85. Elgrishi, N., et al., *A practical beginner's guide to cyclic voltammetry*. Journal of chemical education, 2018. **95**(2): p. 197-206.
86. Gupta, V.K., et al., *Voltammetric techniques for the assay of pharmaceuticals—a review*. Analytical biochemistry, 2011. **408**(2): p. 179.

87. Williams, A.T.R., S.A. Winfield, and J.N. Miller, *Relative fluorescence quantum yields using a computer-controlled luminescence spectrometer*. *Analyst*, 1983. **108**(1290): p. 1067-1071.
88. Taniguchi, M. and J.S. Lindsey, *Database of absorption and fluorescence spectra of > 300 common compounds for use in photochem CAD*. *Photochemistry and photobiology*, 2018. **94**(2): p. 290-327.
89. Limited, H.S.H.U., *A guide to recording fluorescence quantum yields*. N/A: p. 1-6.
90. Leadley, D. *Transmission Electron Microscopy (TEM)*. 2010 4 January 2010 [cited 2022 23 February]; Available from: <https://warwick.ac.uk/fac/sci/physics/current/postgraduate/regs/mpagswarwick/ex5/techniques/structural/tem/>.
91. University of California, S.B. *The Transmission Electron Microscope*. 2007 [cited 2022 23 February]; Available from: [https://www.ccber.ucsb.edu/ucsb-natural-history-collections-botanical-plant-anatomy/transmission-electron-microscope#:~:text=Transmission%20electron%20microscopes%20\(TEM\)%20are,how%20small%20a%20cell%20is](https://www.ccber.ucsb.edu/ucsb-natural-history-collections-botanical-plant-anatomy/transmission-electron-microscope#:~:text=Transmission%20electron%20microscopes%20(TEM)%20are,how%20small%20a%20cell%20is).
92. Güzel, E., *Preparation and investigation of aggregation, fluorescence and singlet oxygen generation properties of gallium and metal-free phthalocyanines*. *Journal of the Turkish Chemical Society Section A: Chemistry*, 2019. **5**(3): p. 1051-1060.
93. Van Mingroot, H., et al., *The emission at 669 nm of metal free phthalocyanine in toluene and 1-bromonaphthalene solutions*. *Chemical physics letters*, 1996. **253**(5-6): p. 397-402.
94. Wu, L., et al., *Helical Nanostructures Self-Assembled from Optically Active Phthalocyanine Derivatives Bearing Four Optically Active Binaphthyl Moieties: Effect of Metal– Ligand Coordination on the Morphology, Dimension, and Helical Pitch of Self-Assembled Nanostructures*. *Langmuir*, 2010. **26**(10): p. 7489-7497.
95. Fazzi, D., et al., *Ultrafast internal conversion in a low band gap polymer for photovoltaics: experimental and theoretical study*. *Physical Chemistry Chemical Physics*, 2012. **14**(18): p. 6367-6374.
96. Cruz, R., et al., *Absolute photoluminescence quantum efficiency of P3HT/CHCl3 solution by Thermal Lens Spectrometry*. *Synthetic metals*, 2013. **163**: p. 38-41.
97. Cheng, X., et al., *Characterization of Multiwalled Carbon Nanotubes Dispersing in Water and Association with Biological Effects*. *Journal of Nanomaterials*, 2011. **2011**: p. 1-12.
98. Ghani, F., J. Kristen, and H. Riegler, *Solubility properties of unsubstituted metal phthalocyanines in different types of solvents*. *Journal of Chemical & Engineering Data*, 2012. **57**(2): p. 439-449.
99. Edwards, L. and M. Gouterman, *Porphyryns: XV. Vapor absorption spectra and stability: Phthalocyanines*. *Journal of Molecular Spectroscopy*, 1970. **33**(2): p. 292-310.
100. WIEDERKEHR, N.A., *A model for specific interactions of manganese-phthalocyanine in protic media*. *Eclética Química*, 1999. **24**: p. 45-59.
101. Mühlbacher, D., et al., *High photovoltaic performance of a low-bandgap polymer*. *Advanced Materials*, 2006. **18**(21): p. 2884-2889.
102. Kobayashi, N., et al., *Effect of peripheral substitution on the electronic absorption and fluorescence spectra of metal-free and zinc phthalocyanines*. *Chemistry—A European Journal*, 2003. **9**(20): p. 5123-5134.
103. Güzel, E., et al., *Comparative studies of photophysical and electrochemical properties of sulfur-containing substituted metal-free and metallophthalocyanines*. *Research on Chemical Intermediates*, 2018. **44**(2): p. 971-989.
104. Cook, S., A. Furube, and R. Katoh, *Analysis of the excited states of regioregular polythiophene P3HT*. *Energy & Environmental Science*, 2008. **1**(2): p. 294.
105. Ray, A., K. Santhosh, and S. Bhattacharya, *Spectroscopic and structural insights on molecular assembly consisting high potential zinc phthalocyanine photosensitizer attached to PyC60*

- through non-covalent interaction*. Spectrochimica Acta Part A: Molecular and Biomolecular Spectroscopy, 2015. **135**: p. 386-397.
106. Loutfy, R.O. and J.H. Sharp, *Intermolecular charge transfer complex formation between manganese phthalocyanine and a naphthoquinone derivative*. The Journal of Physical Chemistry, 1978. **82**(26): p. 2787-2789.
107. Karaoğlu, H.P., A. Koca, and M.B. Koçak, *Synthesis, electrochemical and spectroelectrochemical characterization of novel soluble phthalocyanines bearing chloro and quaternizable bulky substituents on peripheral positions*. Dyes and Pigments, 2012. **92**(3): p. 1005-1017.
108. Quinton, D., et al., *Cyclic voltammetry and spectroelectrochemistry of a novel manganese phthalocyanine substituted with hexynyl groups*. Inorganic Chemistry Communications, 2011. **14**(1): p. 330-332.
109. Lever, A., P. Minor, and J. Wilshire, *Electrochemistry of manganese phthalocyanine in nonaqueous media*. Inorganic Chemistry, 1981. **20**(8): p. 2550-2553.
110. Shafiee, A., M.M. Salleh, and M. Yahaya, *Determination of HOMO and LUMO of [6, 6]-phenyl C61-butyric acid 3-ethylthiophene ester and poly (3-octyl-thiophene-2, 5-diyl) through voltametry characterization*. Sains Malaysiana, 2011. **40**(2): p. 173-176.
111. Gayathri, S.S., et al., *Discrete supramolecular donor–acceptor complexes*. Angewandte Chemie International Edition, 2009. **48**(4): p. 815-819.
112. Ibrahim, M., I. Shehatta, and A. Al-Nayeli, *Voltammetric studies of the interaction of lumazine with cyclodextrins and DNA*. Journal of pharmaceutical and biomedical analysis, 2002. **28**(2): p. 217-225.
113. Shah, A., et al., *Voltammetric and spectroscopic investigations of 4-nitrophenylferrocene interacting with DNA*. Spectrochimica Acta Part A: Molecular and Biomolecular Spectroscopy, 2010. **75**(3): p. 1082-1087.
114. Alarifi, S. and D. Ali, *Mechanisms of multi-walled carbon nanotubes–induced oxidative stress and genotoxicity in mouse fibroblast cells*. International Journal of Toxicology, 2015. **34**(3): p. 258-265.
115. Yanagiya, S.-i., et al., *Growth of cobalt-phthalocyanine on kcl (001) substrate and copper-phthalocyanine whisker*. Japanese journal of applied physics, 2004. **43**(11R): p. 7722.
116. Mirzaeian, M., et al., *Mercaptan removal from natural gas using carbon nanotube supported cobalt phthalocyanine nanocatalyst*. Journal of Natural Gas Science and Engineering, 2014. **18**: p. 439-445.
117. Fischer, F.S., et al., *Highly Crystalline Films of PCPDTBT with Branched Side Chains by Solvent Vapor Crystallization: Influence on Opto-Electronic Properties*. Advanced Materials, 2015. **27**(7): p. 1223-1228.